Design of High-Performance Piezoelectric Transformer-Based DC-DC Converters

by

Elaine Ng

S.B. Electrical Engineering and Physics
Massachusetts Institute of Technology, 2021

Submitted to the Department of Electrical Engineering and Computer Science
in partial fulfillment of the requirements for the degree of

Master of Engineering in Electrical Engineering and Computer Science

at the

MASSACHUSETTS INSTITUTE OF TECHNOLOGY

September 2022

Author .....
Department of Electrical Engineering and Computer Science
August 5, 2022

Certified by .....
David J. Perreault
Ford Professor of Electrical Engineering
Thesis Supervisor

Accepted by .....
Katrina LaCurts
Chair, Master of Engineering Thesis Committee

Design of High-Performance Piezoelectric Transformer-Based DC-DC Converters

by

Elaine Ng

Submitted to the Department of Electrical Engineering and Computer Science
on August 5, 2022, in partial fulfillment of the
requirements for the degree of
Master of Engineering in Electrical Engineering and Computer Science

Abstract

Piezoelectric transformers (PTs) are a promising energy storage alternative for power converter miniaturization. PTs offer galvanic isolation and voltage transformation like traditional magnetic transformers, but have more advantageous power scaling properties at low volumes. Despite these advantages, most attempts at magnetic-less PT-based dc-dc converters have limited whole-converter efficiencies. These attempts typically rely on standard resonant converter topologies not designed to effectively utilize PTs, along with off-the-shelf PTs not optimized for dc-dc power conversion.

In this thesis, we propose a two-pronged approach at designing high-efficiency, high-power-density PT-based converters: (1) circuit-level design strategies and (2) component-level design strategies to optimize PT components for power conversion. At the circuit level, we select high-efficiency topologies and switching sequences that most efficiently utilize PTs as sole energy storage components in dc-dc converters. At the component-level, we present geometry conditions that can aid designers in achieving PT components with both high efficiency and high power density. The strategies and analyses presented in this thesis are validated through simulation of an example PT-based converter design.

Thesis Supervisor: David J. Perreault
Title: Ford Professor of Electrical Engineering

Acknowledgments

I first like to thank Jessica Boles for being an invaluable mentor and friend since I started my journey in power electronics research. Her passion and guidance has inspired me pursue a PhD and to continue exploring and contributing to the field.

I also like to thank my thesis supervisor, Prof. David Perreault, for being a wonderful teacher and advisor. I am grateful to have learned power electronics from him and for all the opportunities and advice he has given me as a fledgling researcher.

I like to thank Prof. Jeffery Lang for all of his helpful advice and suggestions through all of my projects.

I also like to thank my family for all their support throughout my time at MIT and their continued support for my next chapter as a PhD student.

Finally, I like to thank my lab-mates in 10-061 and my friends on C4 for cheering me on through the end of this thesis! Special thanks to my housemates for putting up with my complaints about writing and making sure I was eating during the last weeks of writing this thesis.

Contents

List of Figures

List of Tables

Chapter 1

Introduction

The drive to miniaturize power converters is inhibited by traditional energy storage components such as capacitors and magnetics. Magnetics, in particular, pose fundamental limits to converter miniaturization since their power densities and efficiency capabilities decrease at small scales [25, 51, 53, 61]. Piezoelectrics have emerged as a promising alternative energy storage mechanism [35]. Piezoelectric devices convert energy between the electrical and mechanical domains and store energy in their mechanical compliance and inertia. The high power densities and performance capabilities of piezoelectrics at low volumes make them more conducive to smaller volume power converters than magnetics. Piezoelectrics can come in the form of single-port **piezoelectric resonators (PRs)** or multi-port **piezoelectric transformers (PTs)** as shown in Fig. 1-1 and 1-2. Beyond these efficiency and power density advantages, PRs and PTs can have planar form factors, be batch-fabricated, and may be more amenable to integration than magnetics. PTs have additional advantages including inherent voltage transformation and — in some cases — galvanic isolation, These advantages make PTs extremely promising for applications that require higher conversion ratios and/or isolation.

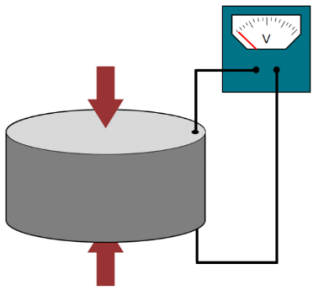

Figure 1-1: Illustration of a piezoelectric resonator (PR)

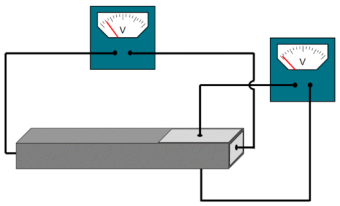

Figure 1-2: Illustration of a two-port piezoelectric transformer (PT)

1.1 Brief History of the Use of PTs in Power Conversion

In the late 1920s and early 1930s, Alexander McLean Nicolson created the first piezoelectric transformers out of Rochelle salt single crystals, one of the only piezoelectric available materials at the time [63]. With the development of more ferroelectric ceramics in the 1940s and 1950s, Charles Abraham Rosen[1] developed the popular Rosen-type PT structure using $BaTiO_3$ ceramics and theory developed by Warren Mason. In the 1990s, new and more reliable piezoelectric materials and fabrication technology allowed the commercial introduction of PTs. They were commonly used to generate high voltage for cold cathode fluorescent lamps (CCFLs) in the late 1990s and early 2000s until the advent of LEDs made such designs obsolete. These early PT-based converters relied on resonant converter topologies and frequency control techniques. Since the decline of CCFLs, PTs have seen little use in power conversion, despite their potential advantages [63].

When driven with ideal sinusoidal inputs, conventional PT efficiencies are known to exceed 95% [60]. However, many PT-based dc-dc converter designs without auxiliary magnetics, have historically produced much lower whole-converter efficiencies as summarized in Table 1.1. These designs are often based on standard resonant converter topologies and control which are not optimized to effectively use the PT.

[1]Rosen also developed other PT structures and has had a tremendous impact on the development of PTs in general. Unfortunately, his work on PTs garnered little attention at the time, so he eventually switched his focus to artificial intelligence.

The focus of many of these previous studies have been on control techniques such as burst-mode control and forward conduction mode control [55, 62]. Other works on the design of PT-based converters include [3–5, 12–16, 18–20, 23, 24, 26–32, 37, 39–43, 46, 48–50, 56–58, 64–74], but a major opportunity exists in investigating converter topologies and operating modes that utilize PT components more efficiently.

Reference	Topology	Efficiency (%)
Rødgaard 2015 [54]	Half-bridge (input) + Half-bridge (output)	70
Rødgaard 2012 [55]	Half-bridge (input) + Half-bridge (output)	68
Sanz 2003 [60]	Half-bridge (input) + Full-bridge (output)	62
Vasic 2013 [62]	Half-bridge (input) + Full-bridge (output)	78

Table 1.1: Whole-converter efficiencies of previous PT-based converters in literature. These designs used topologies that were combinations of half bridge(s) or full bridge(s). Here, we have indicated which topology is used at the input port and output ports of the PT.

Because of their limited commercial use, little is known about how to design PT components themselves for power conversion, especially for use without magnetics. For example, the "datasheet" of a common commercial PT only provides the resonant frequency, nominal operating voltages and power levels, and equivalent circuit parameters for some undefined operating point [1]. These commercial PT components are often only designed for applications like driving CCFL backlights and not optimized for other power conversion applications. Thus, in addition to topologies and operating modes, there is also great potential for improving the power conversion capabilities of PT components themselves by optimizing their design.

While information about PT design is limited, several works (especially in more recent years) have proposed designs for single layer PTs in [33], multilayer PTs in [17], and tunable PTs in [34, 36]. Analysis methods and programs for designing PTs have been proposed in [21, 59]. [22, 45] have also investigated the consequences of secondary effects such as electrode placement and spurious modes on the performance of PTs.

1.2 Previous Works from Our Group in Designing PR-based Converters

While the focus of this thesis is on the design of PT-based converters, much of the theory presented in this thesis is based on our group's previous works in designing PR-based converters and PR components. This section provides a brief summary of the important concepts and results from these works, but more details (especially on how these concepts are adapted for PTs) will be provided in Chapters 2 and 3.

[10, 11] present converter implementations for dc-dc converters that rely on only PRs for energy storage and that have been constrained to use the PR efficiently. Key to efficient PR utilization are specific "switching sequences", which dictate the states of all the switches of a particular topology throughout the PR's resonant cycle, in addition to the circuit topologies. These proposed switching sequences introduce some complexity to the control of the PR converter but ensure that the converter exhibits high efficiency behaviors including zero voltage switching (ZVS), soft charging of the PR, and maximal utilization of the PR's resonant cycle. Analysis techniques based on the PR's charge displacement to predict the behavior of the converter and metrics like efficiency are also provided. These analysis techniques are expanded upon for PT-based converters in Chapter 2. Finally, [11] validates one of these topologies and switching sequences with a prototype PR-based converter capable of reaching efficiencies greater than 99%. [52] proposes a closed-loop control scheme to implement these switching sequences, which require simultaneous control of duty cycle, dead time, and frequency. Chapter 3 presents analogous switching sequences for PT-based converters that effectively utilize the PT.

[7, 8] derive figures of merit for the efficiency and power density capabilities of piezoelectric materials for their use in PRs for power conversion. These figures of merit, which only depend on material properties, can be used to evaluate different materials and vibrational modes. Geometry conditions to reach maximum efficiency and power density are also provided and can be used to guide PR component design. These figures of merit and geometry conditions are expanded upon for PT components

in Chapters 4, 5, 6, and 7.

1.3 Outline of Thesis

The goal of this thesis is to provide strategies for designing high-efficiency, high-power-density PT-based dc-dc converters by optimizing design on two levels: (1) the circuit level and (2) the component level. At the circuit level, we enumerate and downselect topologies and switching sequences to suit the needs of the PT and ensure the PT-based converter exhibits high-efficiency behaviors. At the component level, we constrain the geometry of the PT component to optimize for metrics like efficiency and power density.

Chapter 2 provides important theory that is fundamental to both circuit-level and component-level design. Chapter 3 focuses on circuit-level design for PT-based converters with high-efficiency topologies and switching sequences. Chapter 3 also shows the improved efficiency capabilities of a prototype PT-based converter that realizes one of these promising switching sequences.

Chapters 4, 5, 6, and 7 are devoted to PT component design, assuming one of the highest-efficiency PT-based switching sequences. Chapter 4 explains the $k_{33} - k_{33}$ structure, the PT structure used in this theoretical study. This chapter also derives the reduced Mason model, an equivalent circuit representation assumed for our optimization process, for the $k_{33} - k_{33}$ structure. Chapter 5 derives the maximum efficiency and its geometry condition to aid maximum efficiency PT design. This maximum efficiency geometry condition depends on the converter's intended operating point and can only be physically achieved if ZVS is maintained at this operating point. Chapter 6 derives the geometry condition for maintaining ZVS at the maximum-efficiency operating point. Chapter 7 derives the maximum power density geometry condition.

Chapter 8 proposes a process for designing a PT based on the geometry conditions derived in the previous chapters. This PT design is then combined with a high-efficiency topology and switching sequence to create a full design for a PT-based converter. This proposed design process is validated by simulations of an example

PT-based converter.

Chapter 2

Background Theory and Terminology

In this chapter, we introduce background theory and terminology fundamental to the analyses presented in subsequent chapters.

2.1 Reduced Mason Model for a PT

PTs store energy in the mechanical compliance and inertia of a piezoelectric material. For circuit analysis, it is common to use the "**reduced Mason model**" to represent a PT [44]. The reduced Mason model is the equivalent circuit shown in Fig. 2-1. It includes two terminal capacitances C_{pA} and C_{pB}, which are related to the physical capacitances of the two ports of the PT. There is also a series RLC branch to model the PT's mechanical resonance properties and an ideal transformer to model the voltage transformation provided by the PT. Fig. 2-2 shows the reduced Mason model for a non-isolated PT, which is identical to the model for the isolated PT except for the common node C between the primary and secondary ports. Each of the circuit parameters in the reduced Mason model depends on geometry and material properties of the PT. Chapter 4 shows how to derive these parameters from the constitutive piezoelectric equations.

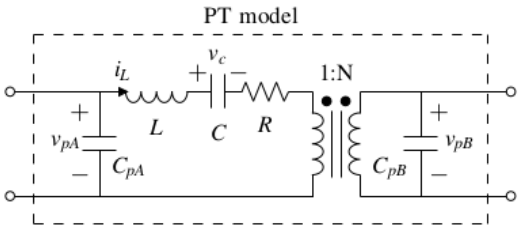

Figure 2-1: Reduced Mason model for an isolated PT

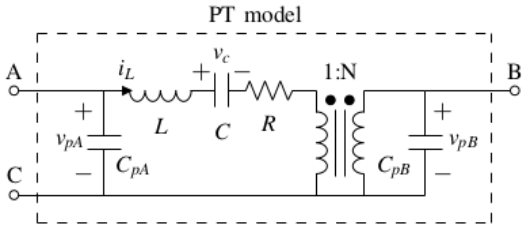

Figure 2-2: Reduced Mason model for a non-isolated PT

2.2 Switching Sequences

To derive high-performance PT-based converter design strategies, we systematically enumerate and downselect topologies and switching sequences that effectively utilize the PT [9]. To do this, we start with the most general case consisting of a PT, a DC source V_{in}, and constant-voltage load V_{out} as shown in Fig. 2-3. (Although Fig. 2-3 shows an isolated PT and an isolated source-load system, all of the following applies to non-isolated systems as well.) With this source-load system, we identify "**stages**" of a switching cycle. Each possible way of connecting the terminals of the PT to the source-load system is considered a stage. We identify stages **for each port of the PT independently**, and we label each stage by the voltage across its corresponding port, v_{pA} or v_{pB}. The polarity of i_L in each stage is constrained for high-efficiency behaviors including all-positive instantaneous power transfer from the input and to the output, minimal charge circulation, and ZVS. Stages can be classified as:

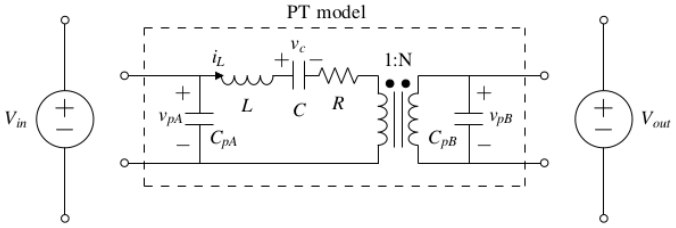

Figure 2-3: Isolated source-load system with isolated PT represented by the reduced Mason model

- *Connected stages*: the PT port is connected to the source-load system such that $v_{pA} = \pm V_{in}$ or $v_{pB} = \pm V_{out}$. The polarity of i_L is constrained for all-positive instantaneous power transfer.

- *Zero stages*: the PT port is short-circuited. The polarity of i_L is constrained to be unidirectional during a stage to avoid excess charge circulation. We designate a zero stage as $Zero+$ or $Zero-$ depending upon the sign of i_L.

- *Open stages*: the PT port is open-circuited, allowing v_{pA} and v_{pB} to charge or discharge through resonance. The polarity of i_L is constrained for ZVS.

Connected stages allow the PT to interact with the source-load system. Zero and open stages are necessary for redistributing energy within the PT. We can create "**sub-sequences**" by permuting stages together to dictate the switching states throughout a resonant cycle for a single port, since stages are defined with respect to a single port. A full "**switching sequence**" is created by combining an input port sub-sequence and an output port sub-sequence. We name switching sequences with the following format: "input port sub-sequence | output port sub-sequence." In this naming convention, we have also assumed that an open stage occurs between each named connected/zero stage. For example, the stages of the output port sub-sequence of $V_{in}, -V_{in}|V_{out}, -V_{out}, Zero+$ are V_{out}, $-V_{out}$, and $Zero+$. This output port sub-sequence is an example of a 6-stage sequence including the unnamed open stages. Chapter 3 goes into the details and results of the actual enumeration and downselection process for topologies and switching sequences.

Since stages only reflect the switching states of the ports independently, we use the term "**terminal configuration**" to refer to the switching states of the entire PT. Terminal configurations are further explained in Chapter 3. As an example, we walk through the operation of the $V_{in}, -V_{in}|V_{out}, -V_{out}, Zero+$ isolated switching sequence shown by Fig. 2-4. In terminal configuration 1, we begin with $v_{pA} = V_{in}$ and the output port is short-circuited. Then in terminal configuration 2, the input port remains at V_{in}, while the output port is open to allow v_{pB} to resonate from 0 to V_{out}. In terminal configuration 3, there are connected stages at both ports ($v_{pA} = V_{in}, v_{pB} = V_{out}$). The current directions allow for energy to be sourced from the input and also delivered to the output. Next in terminal configuration 4, the input port goes through an open stage to resonate v_{pA} from V_{in} to $-V_{in}$, while the

output remains at V_{out}. In terminal configuration 5, the output port goes through another open stage to resonate v_{pB} from V_{out} to $-V_{out}$, while the input remains at $-V_{in}$. Terminal configuration 6 is the second terminal configuration where connected stages occur at both ports ($v_{pA} = -V_{in}, v_{pB} = -V_{out}$). In terminal configuration 7, the input port goes through an open stage for v_{pA} to resonate from $-V_{in}$ up to V_{in}. Finally, in terminal configuration 8, the output port goes through a final open stage to resonate v_{pB} from $-V_{out}$ to 0.

2.3 Charge Transfer Utilization Factors (K_A and K_B)

Since the quality factors of piezoelectric materials are quite high, we assume i_L in the reduced Mason model to be sinusoidal [9]. We can track the charge transferred through each stage of a periodic steady-state switching cycle using the area under the i_L curve shown in Fig. 2-5. In the following sections, we present a few useful metrics and concepts that can be expressed or understood by these charge transfer quantities. First, we present charge transfer utilization factors to quantify how "effectively" a sub-sequence utilizes the PT's resonant cycle. We define the charge transfer utilization factors for each port's sub-sequence separately. For example, K_A is the charge utilization factor for the input port and is defined to be the proportion of charge transferred through connected/zero stages of the input port's sub-sequence that sources energy from the source V_{in}. (There is no charge transfer between the PT and source-load system in open stages.) Similarly, K_B is the proportion of charge transferred through connected/zero stages that delivers energy to the load.

As an example, we calculate K_B for the $V_{in}, -V_{in}|V_{out}, -V_{out}, Zero+$ switching sequence (the same switching sequence used in the last subsection) to be:

$$K_B = \frac{Q_{conn,delivered} + Q_{zero,delivered}}{Q_{conn,total} + Q_{zero,total}} = \frac{|q_{V_{out}}| + |q_{-V_{out}}|}{|q_{V_{out}}| + |q_{-V_{out}}| + |q_{Zero+}|} \tag{2.1}$$

For non-isolated switching sequences, the common node C in Fig. 2-2 introduces dependence between the two ports. Since some of these switching sequences require

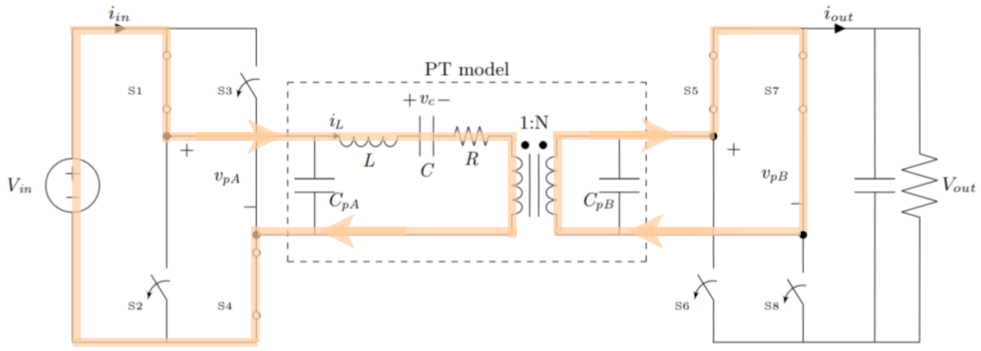

(a) Terminal Configuration 1: $v_{pA} = V_{in}, v_{pB} = Zero+$

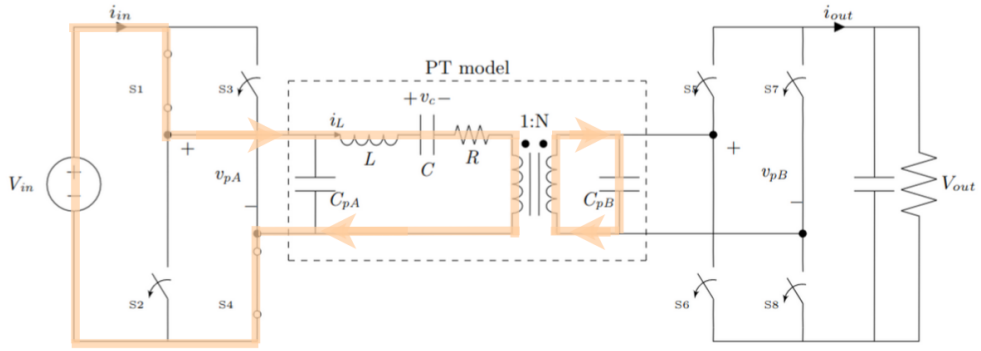

(b) Terminal Configuration 2: $v_{pA} = V_{in}, v_{pB} = Open$

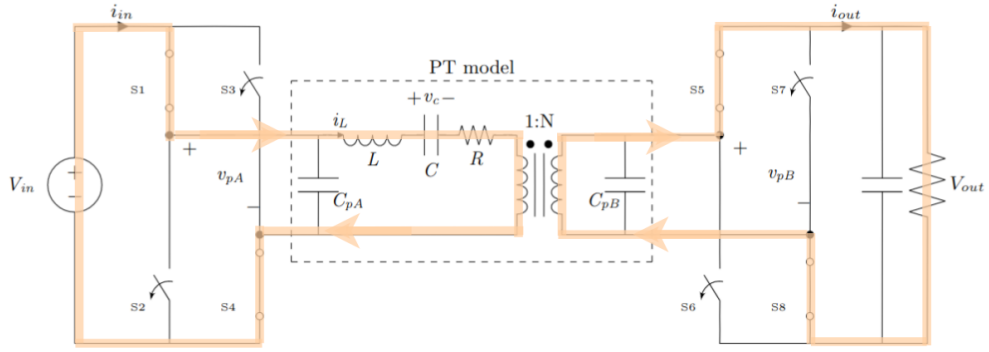

(c) Terminal Configuration 3: $v_{pA} = V_{in}, v_{pB} = V_{out}$

Figure 2-4: Terminal Configurations of $V_{in}, -V_{in}|V_{out}, -V_{out}, Zero+$: The voltages v_{pA} and v_{pB} are labeled to show that this switching sequence exhibits all the voltages in its name. Current directions are indicated by the orange arrows.

the output terminal B to connect to V_{in}, we also differentiate between K_{Bin} and K_{Bout}. K_{Bin} is the fraction of connected/zero stage charge transfer sourced from the input port by terminal B, while K_{Bout} refers to terminal B delivering energy to V_{out}. K_{Bin} may be positive or negative depending on if terminal B contributes to or counters energy sourced from V_{in}, respectively [9].

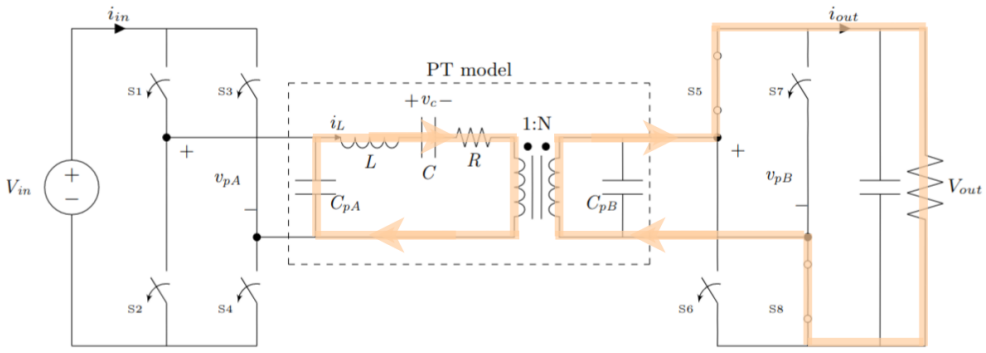

(d) Terminal Configuration 4: $v_{pA} = Open, v_{pB} = V_{out}$

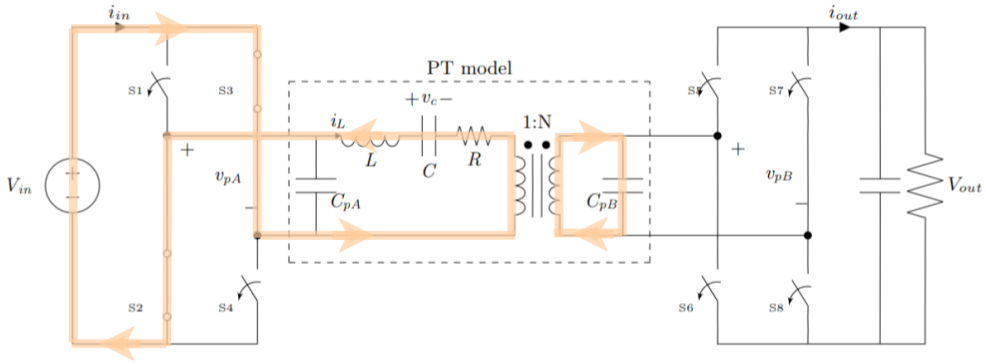

(e) Terminal Configuration 5: $v_{pA} = -V_{in}, v_{pB} = Open$

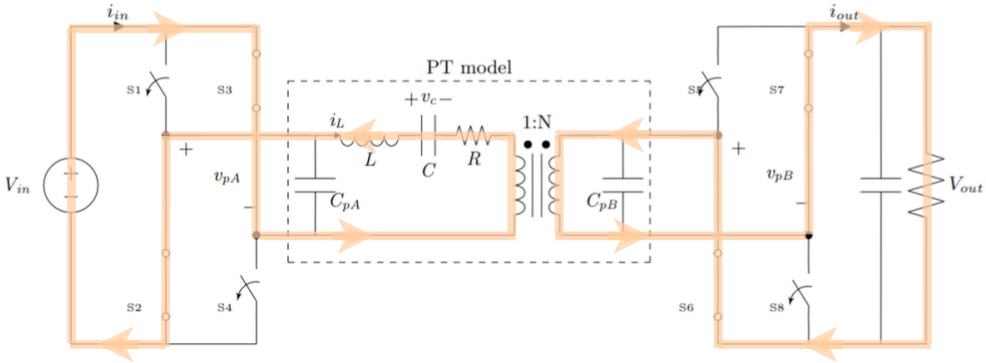

(f) Terminal Configuration 6: $v_{pA} = -V_{in}, v_{pB} = -V_{out}$

Figure 2-4: (Continued) Terminal Configurations of $V_{in}, -V_{in}|V_{out}, -V_{out}, Zero+$: The voltages v_{pA} and v_{pB} are labeled to show that this switching sequence exhibits all the voltages in its name. Current directions are indicated by the orange arrows.

Because the converter operates in periodic steady state (PSS), the total net charge transferred in one cycle must be zero. This means that the total charge delivered in stages with $+i_L$ polarity must equal to the total charge delivered in stages with $-i_L$ polarity. Thus for our example switching sequence, $V_{in}, -V_{in}|V_{out}, -V_{out}, Zero+$, the

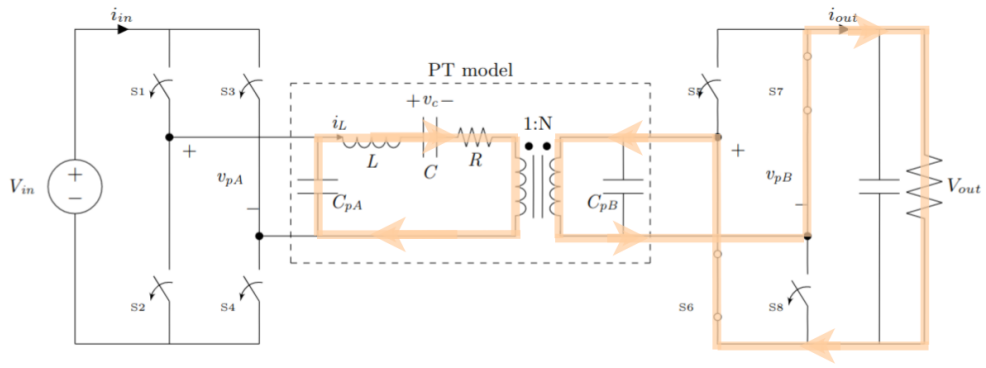

(g) Terminal Configuration 7: $v_{pA} = Open, v_{pB} = -V_{out}$

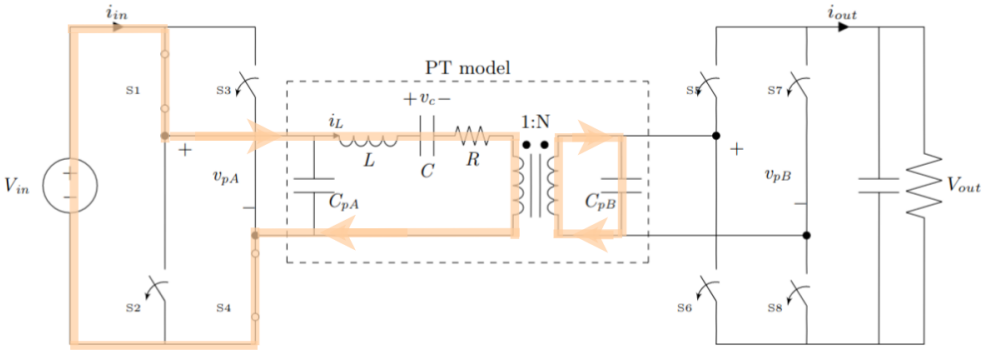

(h) Terminal Configuration 8: $v_{pA} = V_{in}, v_{pB} = Open$

Figure 2-4: (Continued) Terminal Configurations of $V_{in}, -V_{in}|V_{out}, -V_{out}, Zero+$: The voltages v_{pA} and v_{pB} are labeled to show that this switching sequence exhibits all the voltages in its name. Current directions are indicated by the orange arrows.

following conservation of charge equation holds for the output port:

$$|q_{V_{out}}| + |q_{Zero+}| = |q_{-V_{out}}| \tag{2.2}$$

(2.2) implies that $|q_{V_{out}}|$ can range from 0 to $|q_{-V_{out}}|$, which constrains K_B defined by (2.1) to the range $\frac{1}{2} < K_B < 1$. An analogous calculation yields $K_A = 1$ for the input sub-sequence.

Sub-sequences that consist of four stages have constant charge utilization factors. When the range for a charge utilization factor is fixed to a constant, the sub-sequence circulates minimum excess charge, which improves PT efficiency. On the other hand, sub-sequences that consist of six or more stages allow for an unfixed range for their respective charge utilization factors. These ranges indicate that the converter is able to regulate over a wider range of voltage conversion ratios. The switching sequences

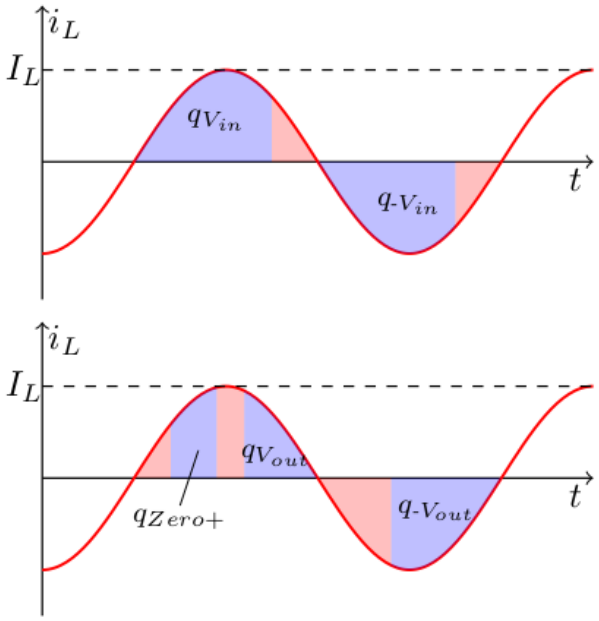

Figure 2-5: Sinusoidal approximation of i_L. The charge transfer of each stage is shaded from the perspective of the input port (top) and the output port (bottom). The switching sequence shown here is the isolated switching sequence $V_{in}, -V_{in}|V_{out}, -V_{out}, Zero+$

shown in Chapter 3 are combinations of four-stage and six-stage sub-sequences to achieve regulation with high efficiency over a wide range of voltage gains.

2.4 Amplitude of Resonance Model

The amplitude of resonance I_L, defined as the amplitude of i_L in the reduced Mason model, is an extremely useful quantity as it can be used to estimate many relevant metrics, such as efficiency. Since i_L is assumed to be sinusoidal and the timing of six-stage switching sequences is fully constrained as later discussed in Chapter 3, the total charge transferred through all of the stages of a switching sequence, Q_{total}, is the integral of the magnitude of i_L over a full switching cycle. I_L can be calculated from Q_{total} as:

$$I_L = \frac{\pi}{2} f Q_{total} \tag{2.3}$$

Q_{total} can be calculated with respect to either port. With respect to the input port, Q_{total} for isolated switching sequences is:

$$Q_{total} = \frac{P_{out}}{fK_AV_{in}} + 2C_{pA}V_{ppA} \tag{2.4}$$

where the first term of (2.4) is the total charge transferred during connected/zero stages, and the second term is the total charge transferred during open stages [9]. For non-isolated switching sequences, Q_{total} with respect to the input port is:

$$Q_{total} = \frac{\frac{P_{out}}{fV_{in}} + 2K_AC_{pA}V_{ppA} + 2K_{Bin}C_{pB}V_{ppB}}{K_A + \frac{K_{Bin}}{N}} \tag{2.5}$$

With respect to the output port, Q_{total} is:

$$Q_{total} = N\Big(\frac{P_{out}}{fK_BV_{out}} + 2C_{pB}V_{ppB}\Big) \tag{2.6}$$

Because we can use either port to calculate I_L, it is often simpler to use the port whose charge utilization factor is fixed (when one of the ports has a 4-stage sequence). For example if K_A is fixed, I_L can be expressed as:

$$I_L = \pi\Big(\frac{P_{out}}{2K_AV_{in}} + fC_{pA}V_{ppA}\Big) \tag{2.7}$$

2.5 PT Efficiency Estimation

In this section, the method of estimating PT efficiency is introduced. More details will be provided in Chapter 5. The mechanical efficiency of the PT (η) for any operating point can be estimated using the amplitude of resonance, I_L, as:

$$\eta = \frac{P_{out}}{P_{out} + P_{loss}} = \frac{P_{out}}{P_{out} + \frac{1}{2}I_L^2R} \tag{2.8}$$

We seek to maximize PT efficiency, which is equivalent to minimizing the loss ratio P_{loss}/P_{out}:

$$\frac{P_{loss}}{P_{out}} = \frac{\frac{1}{2}I_L^2 R}{P_{out}} \tag{2.9}$$

η can be equivalently written in terms of the loss ratio as:

$$\eta = \frac{1}{1 + \frac{P_{loss}}{P_{out}}} \tag{2.10}$$

In Chapter 5, we use the reduced Mason model to express this loss ratio in terms of geometry and material properties. Then, we will constrain the geometry of the PT to reach a minimum loss ratio (or maximum efficiency) at a specified operating point.

2.6 Zero Voltage Switching (ZVS) Region

By definition, Q_{total} with respect to the input port should be the same as Q_{total} with respect to the output port, as both are based on I_L. Thus, the following equation must hold for isolated switching sequences:

$$\frac{P_{in}}{fK_A V_{in}} + 2C_{pA}V_{ppA} = N\Big(\frac{P_{out}}{fK_B V_{out}} + 2C_{pB}V_{ppB}\Big) \tag{2.11}$$

And equivalently for non-isolated switching sequences:

$$\frac{\frac{P_{out}}{fV_{in}} + 2K_A C_{pA}V_{ppA} + 2K_{Bin}C_{pB}V_{ppB}}{K_A + \frac{K_{Bin}}{N}} = N\Big(\frac{P_{out}}{fK_B V_{out}} + 2C_{pB}V_{ppB}\Big) \tag{2.12}$$

Any differences can only be compensated by the ranges of the charge utilization factors [9]. Thus, these ranges dictate a switching sequence's ZVS region. Given the parameters of a PT, we can map the ZVS region of a switching sequence using (2.11) or (2.12). Fig. 2-6 plots the ZVS region for a few isolated switching sequences. Note that the maximum efficiency introduced in Section 2.5 can only be achieved if the operating point corresponding to that maximum is inside the ZVS region.

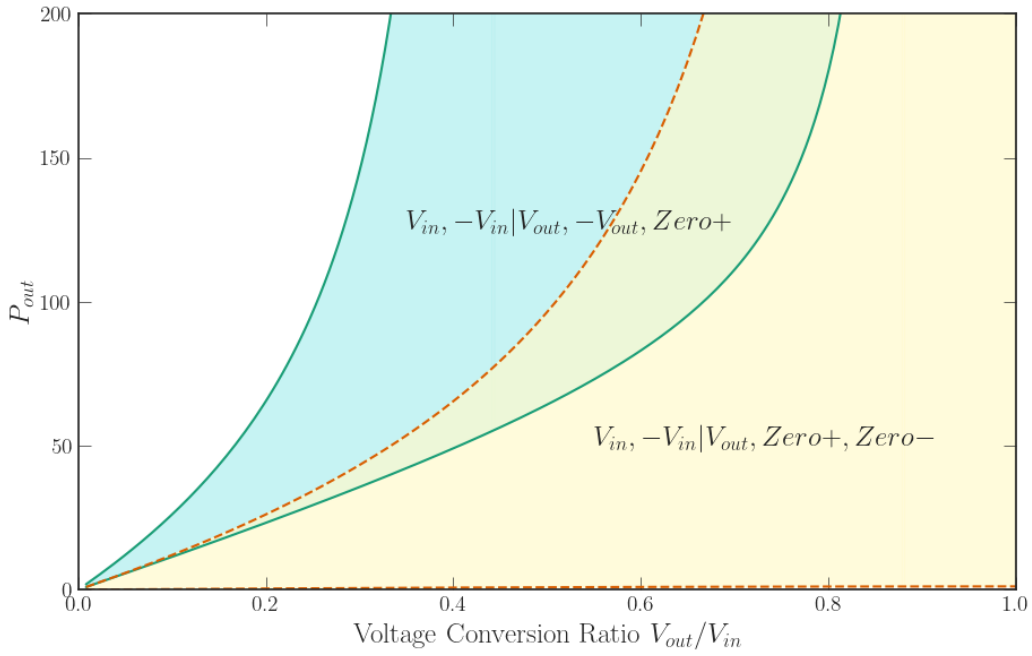

Figure 2-6: ZVS regions for the labeled isolated switching sequences given the parameters of the PT designed in Chapter 8 in Table 8.2 and $V_{in} = 100\,\mathrm{V}$

Chapter 3

Circuit-Level Design

To identify high-efficiency PT-based converter topologies and switching sequences, we begin with a general source-load system and PT modeled as shown in Fig. 2-3. We then enumerate all the possible topologies and switching sequences. With this exhaustive list of switching sequences, we undertake a systematic downselection process using a set of constraints based on desired behaviors for the converter. Enumeration can be done by either considering (1) stages first or (2) topologies first. Stage-based enumeration is easier to conceptualize for isolated switching sequences, while topology-based enumeration is easier to conceptualize for non-isolated switching sequences. However, both approaches can be used regardless if the converter is isolated or non-isolated as both lead to the same final set of optimized topologies and switching sequences given the same downselection steps. The first two sections of this chapter cover the enumeration and downselection process. The final section presents results from our prototype PT-based converter that implements one proposed non-isolated switching sequence and topology.

3.1 Stage-Based Enumeration and Downselection

Since stages are defined with respect to a port, stage-based enumeration is helpful for enumerating isolated switching sequences, since one may easily consider each port separately [9]. In this approach, stages are first identified as described in Section 2.2.

Then, the polarity of i_L is constrained to be unidirectional in these stages as follows:

- For connected stages: the polarity of i_L is constrained for *all-positive instantaneous power transfer*, meaning energy is always instantaneously transferred unidirectionally from a source or to a load.
- For open stages: the polarity of i_L is constrained so each port's voltage can increase/decrease to reach its next-stage voltage for ZVS.

Table 3.1 shows the i_L polarity constraints for stages for an isolated converter. As an example, we walk through the polarities of the stages in the first three terminal configurations of $V_{in}, -V_{in}|V_{out}, -V_{out}, Zero+$ shown in Fig. 3-1. In these three terminal configurations, the input port only experiences a single connected stage V_{in} which requires $i_L > 0$. In all three circuits of Fig. 3-1, i_L in the input side of the PT is shown pulling energy from the source. On the other hand, the output port transitions from $Zero+$ in terminal configuration 1, to an open stage in terminal configuration 2, and finally V_{out} in terminal configuration 3. $Zero+$ and V_{out} are stages that require $i_L > 0$, and thus the current in the output side of the PT is pushing energy to the load in the circuits for these stages. i_L is in this same forward direction during the open stage in terminal configuration 2 because $\frac{dv_{pB}}{dt} > 0$.

Polarity	Input Stages ($v_{pA} =$)	Output Stages ($v_{pB} =$)
$i_L > 0$	V_{in}; $Zero+$; $\frac{dv_{pA}}{dt} < 0$	V_{out}; $Zero+$; $\frac{dv_{pB}}{dt} > 0$
$i_L < 0$	-V_{in}; $Zero-$; $\frac{dv_{pA}}{dt} > 0$	$-V_{out}$; $Zero-$; $\frac{dv_{pB}}{dt} < 0$

Table 3.1: Potential isolated stages by port and i_L polarity

Next, we permute these stages to create sub-sequences for each port, which are then combined to create full switching sequences. These sub-sequences are downselected according to the following constraints:

1. A minimum number of stages (for control simplicity)
2. At least one connected stage (for transferring energy to/from the PT)
3. Alternating connected/zero stages and open stages (for ZVS between connected/zero stages)

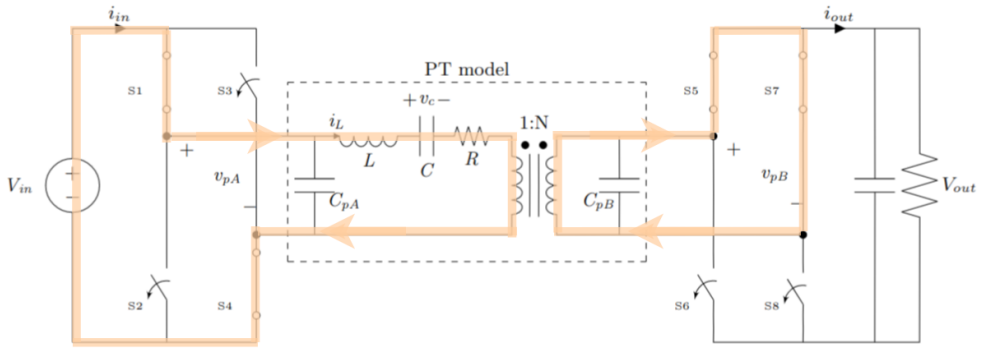

(a) Terminal Configuration 1: $v_{pA} = V_{in}, v_{pB} = Zero+$

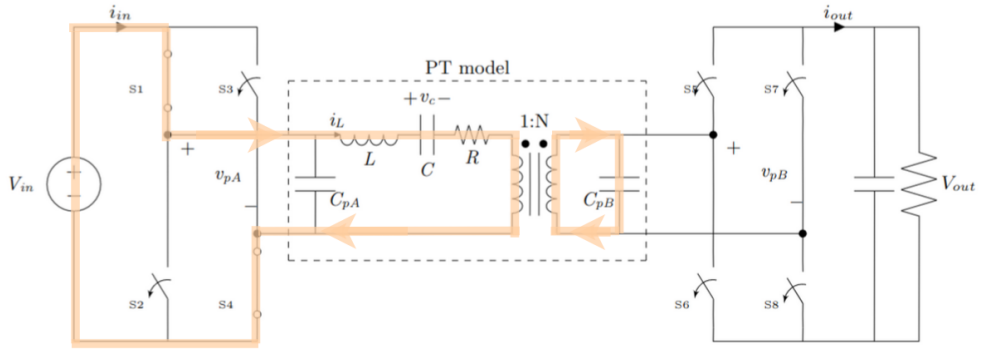

(b) Terminal Configuration 2: $v_{pA} = V_{in}, v_{pB} = Open$

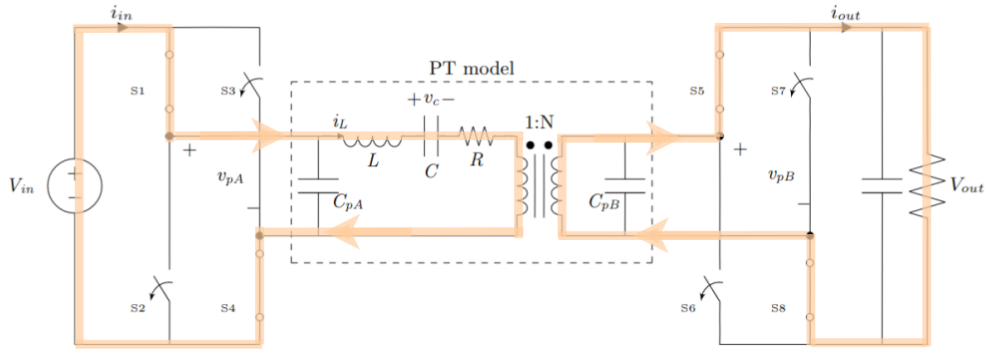

(c) Terminal Configuration 3: $v_{pA} = V_{in}, v_{pB} = V_{out}$

Figure 3-1: First Three Terminal Configurations of $V_{in}, -V_{in}|V_{out}, -V_{out}, Zero+$: Current directions are indicated by the orange arrows, which match the i_L polarity constraints in Table 3.1.

4. No repetition of the same connected/zero stage

5. At least once connected/zero stage each for positive and negative i_L (for charge balance on terminal C across the cycle)

6. One sequential span for each of positive and negative i_L (for completion in one PT resonant cycle)

These constraints are essential for a high-efficiency PT-based converter that is also practical to realize. Lastly, we filter the full switching sequences to be capable of these behaviors from the above set of constraints over a wide range of voltage conversion ratios. We can calculate the ideal voltage conversion range of a switching sequence by analyzing the energy and charge balance within the PT across a resonant cycle. Across a cycle, the energy sourced from V_{in} should be equal to the energy delivered to the load. For example, the conservation of energy equation for the $V_{in}, -V_{in}|V_{out}, -V_{out}, Zero+$ switching sequence is:

$$V_{in}(|q_{V_{in}}| + |q_{-V_{in}}|) = \frac{V_{out}}{N}(|q_{V_{out}}| + |q_{-V_{out}}|) \tag{3.1}$$

where q_n is the charge transferred by i_L during stage n. The conservation of charge equation for this switching sequence, neglecting open stages, is:

$$|q_{V_{in}}| = |q_{-V_{in}}| = |q_{V_{out}}| + |q_{Zero+}| = |q_{-V_{out}}| \tag{3.2}$$

To satisfy (3.2) the following range must also hold:

$$0 \leq |q_{V_{out}}| \leq |q_{V_{in}}| \tag{3.3}$$

Substituting (3.2) and (3.3) into (3.1) yields the following voltage range for the switching sequence:

$$N < \frac{V_{out}}{V_{in}} < 2N \tag{3.4}$$

6-stage sub-sequences are capable of wide voltage conversion ranges but do not fully utilize the PR's connected/zero stage charge displacement for energy transfer [9]. 4-stage sub-sequences can fully utilize the PR's connected/zero stage charge displacement for energy transfer, but are only capable of fixed voltage conversion ratios. To get the benefits of both types of sub-sequences, the final set of isolated switching sequences shown in Table 3.2 are 4x6-stage or 6x4-stage switching sequences. These switching sequences can be realized by the topologies shown in Fig. 3-2.

Table 3.2: Proposed Isolated Switching Sequences, Topologies, and Constraints from [9]

Switching Sequence (Input | Output)	Topology (Fig. 3-2)	Ideal V_{out}/V_{in} Range	Charge Transfer Utilization Factors (K)	C_{pA},C_{pB} Voltage Ranges (V_{ppA}, V_{ppB})
$V_{in}, -V_{in} \| V_{out}, Zero+, Zero-$	3-2a	$2N < \frac{V_{out}}{V_{in}} < \infty$	$K_A = 1, 0 < K_B < \frac{1}{2}$	$2V_{in}, V_{out}$
$V_{in}, -V_{in} \| V_{out}, -V_{out}, Zero+$	3-2d	$N < \frac{V_{out}}{V_{in}} < 2N$	$K_A = 1, \frac{1}{2} < K_B < 1$	$2V_{in}, 2V_{out}$
$V_{in}, Zero- \| V_{out}, Zero+, Zero-$	3-2c	$N < \frac{V_{out}}{V_{in}} < \infty$	$K_A = \frac{1}{2}, 0 < K_B < \frac{1}{2}$	V_{in}, V_{out}
$V_{in}, Zero- \| V_{out}, -V_{out}, Zero+$	3-2b	$\frac{N}{2} < \frac{V_{out}}{V_{in}} < N$	$K_A = \frac{1}{2}, \frac{1}{2} < K_B < 1$	$V_{in}, 2V_{out}$
$V_{in}, -V_{in}, Zero- \| V_{out}, Zero-$	3-2a	$N < \frac{V_{out}}{V_{in}} < 2N$	$\frac{1}{2} < K_A < 1, K_B = \frac{1}{2}$	$2V_{in}, V_{out}$
$V_{in}, -V_{in}, Zero- \| V_{out}, -V_{out}$	3-2d	$\frac{N}{2} < \frac{V_{out}}{V_{in}} < N$	$\frac{1}{2} < K_A < 1, K_B = 1$	$2V_{in}, 2V_{out}$
$V_{in}, Zero+, Zero- \| V_{out}, Zero-$	3-2c	$0 < \frac{V_{out}}{V_{in}} < N$	$0 < K_A < \frac{1}{2}, K_B = \frac{1}{2}$	V_{in}, V_{out}
$V_{in}, Zero+, Zero- \| V_{out}, -V_{out}$	3-2b	$0 < \frac{V_{out}}{V_{in}} < \frac{N}{2}$	$0 < K_A < \frac{1}{2}, K_B = 1$	$V_{in}, 2V_{out}$

3.2 Topology-Based Enumeration and Downselection

For a non-isolated PT and source-load system having common negatives as shown in Fig. 3-3, any of the three PT terminals (A, B, C) can connect to any of the three nodes of the source-load system $(0, 1, 2)$. The common terminal C introduces dependence between the two ports. While stage-based enumeration can be used to enumerate non-isolated switching sequences, it is more straightforward to consider all the topologies for this system rather than enumerating stages for each port [47].

First we identify possible connections to the source-load system for each of the three PT terminals. Each terminal can have:

- one source/load connection to 0, 1, or 2 (three possibilities), creating a fixed node
- two source/load connections switching between $[1, 0]$, $[2, 0]$ or $[1, 2]$ (three possibilities), creating a switch node that requires two unidirectional-blocking switches
- three source/load connections switching between $[0, 1, 2]$ (one possibility), creating a switch node requiring four unidirectional-blocking switches (two for the middle-voltage node connection)

Combinations of the above connections yield almost 300 topologies with < 8 unidirectional-blocking switches. We now filter these topologies with another set of constraints assuming a step-up configuration where $V_{out} > V_{in}$ and $C_{pA} > C_{pB}$:

1. Contains a maximum of five connections to the source-load system across all terminals for simplicity

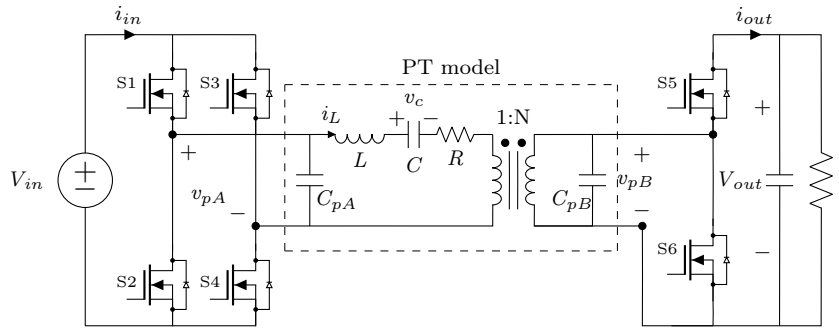

(a) FB-HB

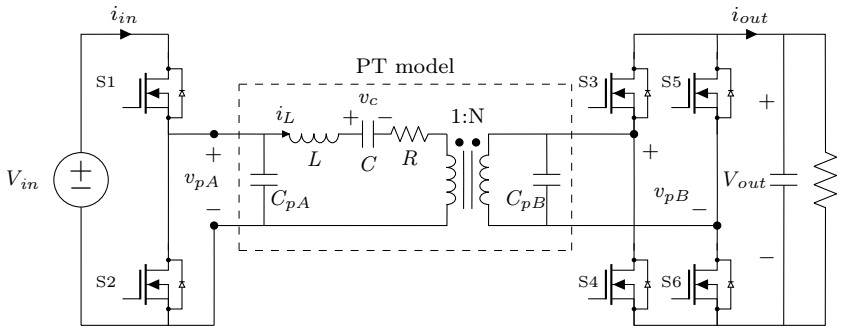

(b) HB-FB

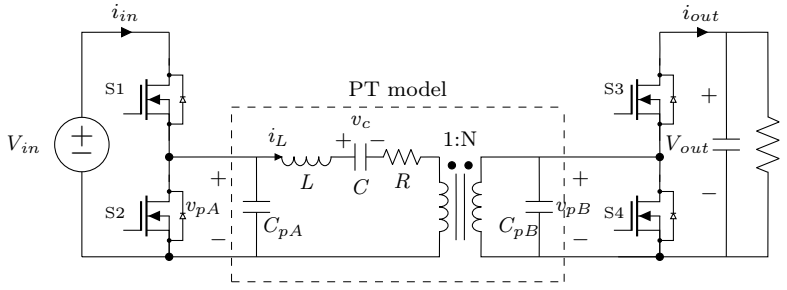

(c) HB-HB

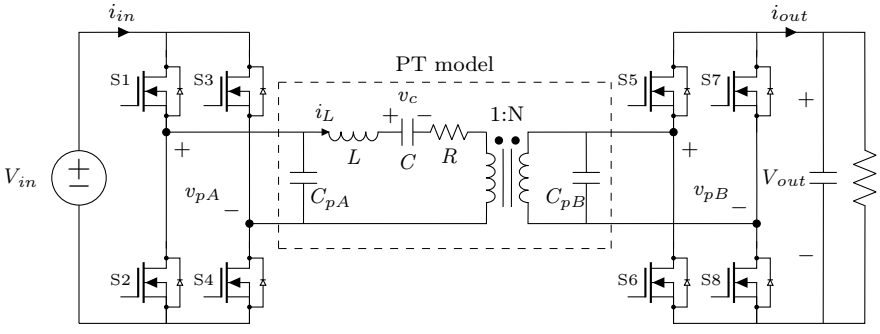

(d) FB-FB

Figure 3-2: Topologies for realizing the isolated switching sequences listed in Table 3.2 from [9]

2. Contains at least one connection to each of V_{in} (1) and V_{out} (2)

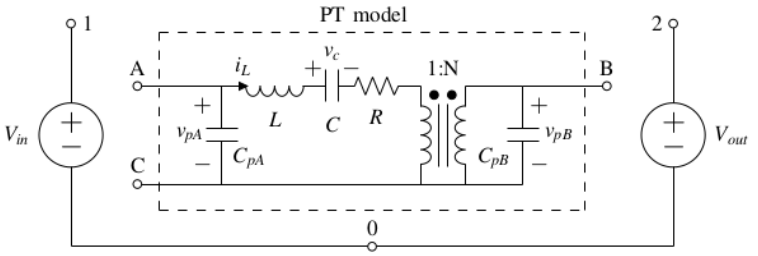

Figure 3-3: Non-isolated PT with non-isolated source-load system

3. Contains no more than 1 fixed terminal

4. Terminals A and C do not connect to V_{out}, since $V_{out} > V_{in}$ and $C_{pA} >> C_{pB}$, (i.e. it would take an impractical length of time for A or C to resonate to V_{out} for ZVS [1])

The downselected topologies are summarized in Fig. 3-4.

We next enumerate *terminal configurations* for each topology. Like the concept of "stage" we used before for each port, a terminal configuration describes how each terminal is connected to the source-load system, but for the entire PT. Terminal configurations can also be classified into *connected* when all terminals are connected to the source-load system or *open* when at least one of the terminals is open. For convenience, we label connected terminal configurations by listing each terminal label (A, B, C) followed by the node it is connected to $(0, 1, 2)$. For example, the terminal configuration $A1B2C0$ has terminal A connected to V_{in} (1), B connected to V_{out} (2), and C connected to Gnd (0). We also constrain the polarity of i_L in connected terminal configurations for all-positive instantaneous power transfer and during open terminal configurations for ZVS. These i_L polarity constraints are summarized in Table 3.3.

After identifying these terminal configurations, we create switching sequences by permuting connected terminal configurations together, assuming an open configuration in between each connected configuration. We can also label a switching sequence by the sequence of terminal configurations. For example, $A0B2C0 - A1B0C0 -$

[1]This constraint is specific to step-up configurations. For step-down configurations, A and C should not connect to V_{in}. $C_{pA} >> C_{pB}$ for the Rosen-type PT, which is a type of PT that is widely available today and the type of PT we used in our prototype in Sec 3.3.)

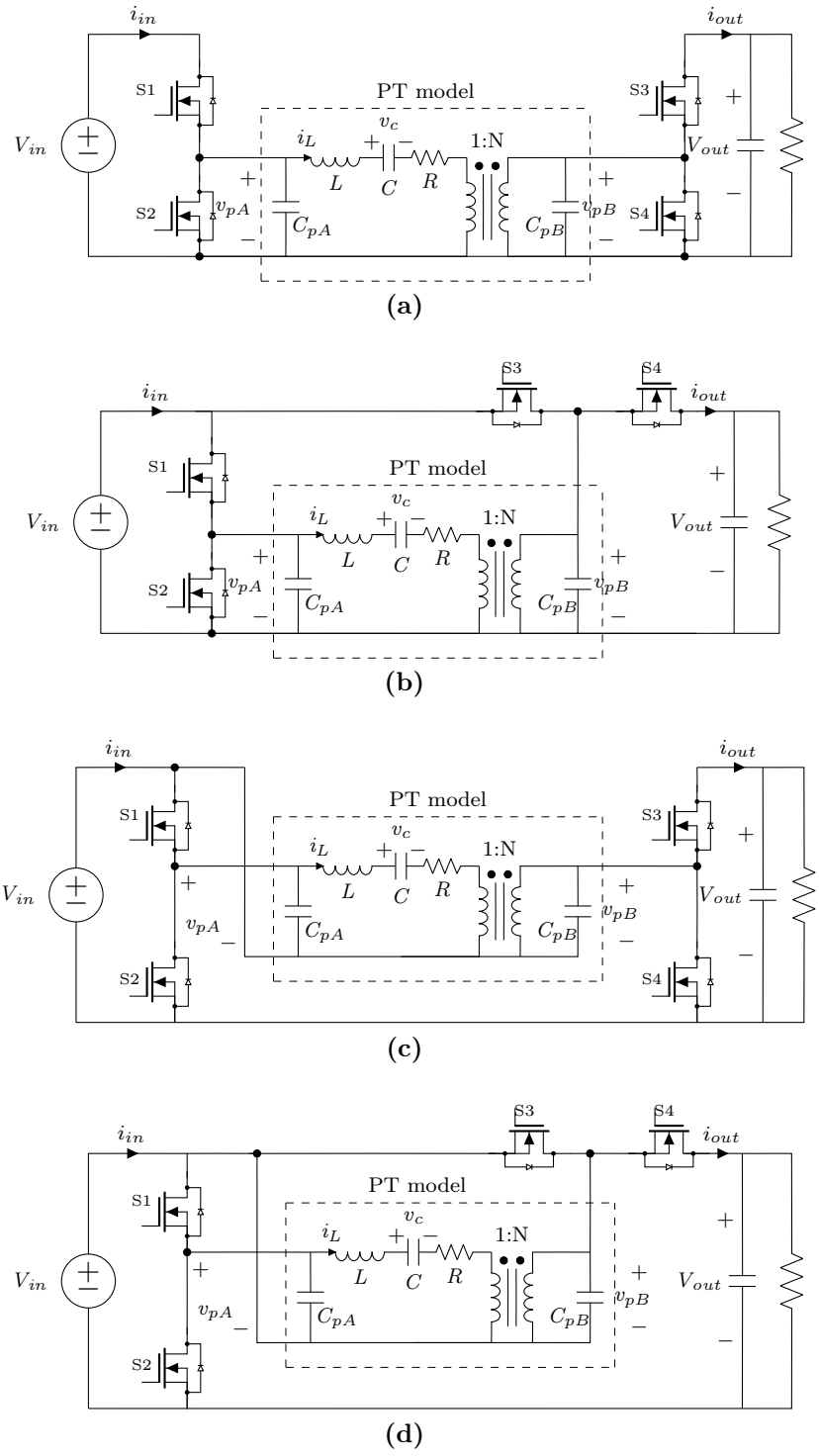

Figure 3-4: Topologies for realizing the non-isolated switching sequences listed in Table 3.4 from [9]

$A0B0C1$ is a switching sequence with six terminal configurations. We focus on switching sequences with six terminal configurations because six is the minimum number

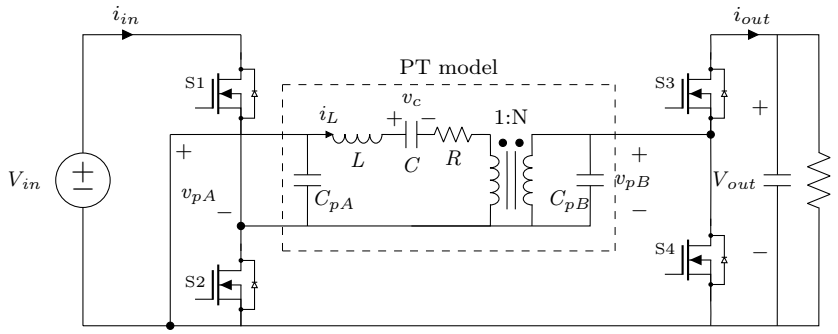

(e)

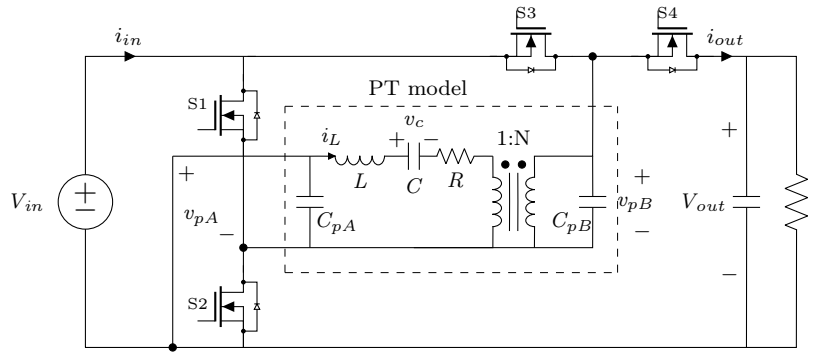

(f)

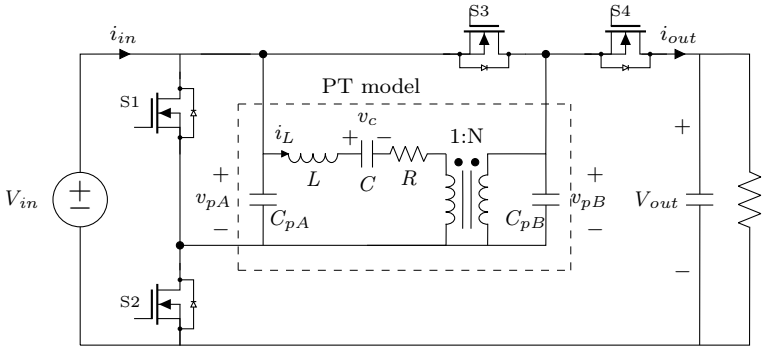

(g)

Figure 3-4: (Continued) Topologies for realizing the non-isolated switching sequences listed in Table 3.4 from [9].

of configurations needed for voltage regulation. This yields 330 distinct switching sequences which we then downselect using the following constraints:

1. At least one configuration of $+i_L$ and one configuration of $-i_L$, for charge balance on terminal C over a cycle.

2. At least two connected terminal configurations with energy transfer, for energy balance within the PT.

Polarity	Terminal Configuration	Terminal Transition (During Open Terminal Configurations)
$i_L > 0$	$A0B2C0, A1B0C0, A1B0C1,$ $A1B1C0, A1B2C0, A1B2C1$	$A1 \rightarrow A0, B0 \rightarrow B2,$ $C0 \rightarrow C1, B1 \rightarrow B2$
$i_L < 0$	$A0B0C1, A0B1C0, A0B1C1$	$A0 \rightarrow A1, B2 \rightarrow B0,$ $C1 \rightarrow C0, B2 \rightarrow B1$
Either	$A0B0C0, A1B1C1$	N/A

Table 3.3: Potential non-isolated configurations by i_L polarity constraints from [9]

3. At least one connection to V_{in} (1) and one connection to V_{out} (2).

4. The required i_L polarities of all the terminal configurations (including open configurations) fit sequentially in one resonant cycle

5. No two terminals are always tied together (or else the PT is effectively a two-terminal device).

6. No repetition of the same terminal configuration.

7. The sequence enables voltage regulation capability beyond fixed voltage conversion ratios.

These switching sequences can also be conceptualized with the naming convention introduced in Section 2.2, by using the voltages of the two ports in each configuration. For example, $A1B2C0 - A0B2C0 - A0B1C0$ creates the $V_{in}, Zero+, Zero-|V_{out}, V_{in}$ switching sequence. We also filter these switching sequences for sequences where only one PT terminal transitions between two connected terminal configurations in a single half-cycle (i.e. between two connected configurations of the same i_L polarity). This leads to 4x6 switching sequences if terminal B is the only terminal allowed to transition like this, 6x4 switching sequences if terminal A is transitioning, and 6x6 switching sequences if terminal C is transitioning. In 4x6 switching sequences, the output port is regulating, while in 6x4 switching sequences, the input port is regulating. For example, in the same switching sequence $A1B2C0 - A0B2C0 - A0B1C0$, terminal A is the only terminal that transitions between two connected configurations of the same polarity ($A1B2C0$ and $A0B2C0$ are both $+i_L$). $A1B2C0-$

$A0B2C0 - A0B1C0$ is also a 6x4 switching sequence that regulates with the input port. The final set of non-isolated switching sequences is shown in Table 3.4. Each of these switching sequences can be implemented by one of the topologies in Fig. 3-4.

Table 3.4: Proposed Non-Isolated Switching Sequences, Topologies, and Constraints from [9]

Switching Sequence (Input | Output)	Topology (Fig. 3-4)	Ideal V_{out}/V_{in}	Charge Transfer Range Utilization Factors (K)	C_{pA},C_{pB} Voltage Ranges (V_{ppA}, V_{ppB})
$V_{in}, Zero+, Zero- \mid$ $V_{out}, Zero-$	3-4a	$0 < \frac{V_{out}}{V_{in}} < N$	$0 < K_A < \frac{1}{2}$ $K_{Bin} = 0, K_{Bout} = \frac{1}{2}$	V_{in}, V_{out}
$V_{in}, Zero+, Zero- \mid$ V_{out}, V_{in}	3-4b	$1 < \frac{V_{out}}{V_{in}} < N+1$	$0 < K_A < \frac{1}{2}$ $K_{Bin} = \frac{1}{2}, K_{Bout} = \frac{1}{2}$	$V_{in}, V_{out} - V_{in}$
$Zero+, -V_{in}, Zero- \mid$ $V_{out} - V_{in}, Zero-$	3-4d	$1 < \frac{V_{out}}{V_{in}} < N+1$	$0 < K_A < \frac{1}{1}$ $K_{Bin} = \frac{1}{2}, K_{Bout} = \frac{1}{2}$	$V_{in}, V_{out} - V_{in}$
$Zero+, -V_{in}, Zero- \mid$ $V_{out}, -V_{in}, Zero-$	3-4e	$0 < \frac{V_{out}}{V_{in}} < N-1$	$0 < K_A < \frac{1}{2}$, $\frac{-1}{2} < K_{Bin} < 0, K_{Bout} = \frac{1}{2}$	$V_{in}, V_{out} + V_{in}$
$Zero+, -V_{in}, Zero- \mid$ $V_{out}, Zero-, V_{in}$	3-4f	$1 < \frac{V_{out}}{V_{in}} < N$	$0 < K_A < \frac{1}{2}$ $0 < K_{Bin} < \frac{1}{2}, K_{Bout} = \frac{1}{2}$	V_{in}, V_{out}
$V_{in}, Zero+, Zero- \mid$ $V_{out}, V_{out} - V_{in}, Zero-$	3-4g	$1 < \frac{V_{out}}{V_{in}} < N$	$0 < K_A < \frac{1}{2}$ $0 < K_{Bin} < \frac{1}{2}, K_{Bout} = \frac{1}{2}$	V_{in}, V_{out}
$V_{in}, Zero- \mid$ $Zero+, V_{out}, Zero-$	3-4a	$N < \frac{V_{out}}{V_{in}} < \infty$	$K_A = \frac{1}{2}$ $K_{Bin} = 0, 0 < K_{Bout} < \frac{1}{2}$	V_{in}, V_{out}
$V_{in}, Zero- \mid$ V_{in}, V_{out}, V_{in}	3-4b	$N+1 < \frac{V_{out}}{V_{in}} < \infty$	$K_A = \frac{1}{2}$ $0 < K_{Bin} < \frac{1}{2}, 0 < K_{Bout} < \frac{1}{2}$	$V_{in}, V_{out} - V_{in}$
$Zero+, -V_{in} \mid$ $-V_{in}, V_{out} - V_{in}, -V_{in}$	3-4c	$N < \frac{V_{out}}{V_{in}} < \infty$	$K_A = \frac{1}{2}$ $K_{Bin} = 0, 0 < K_{Bout} < \frac{1}{2}$	V_{in}, V_{out}
$Zero+, -V_{in} \mid$ $Zero+, V_{out} - V_{in}, Zero-$	3-4d	$N+1 < \frac{V_{out}}{V_{in}} < \infty$	$K_A = \frac{1}{2}$ $0 < K_{Bin} < \frac{1}{2}, 0 < K_{Bout} < \frac{1}{2}$	$V_{in}, V_{out} - V_{in}$
$Zero+, -V_{in} \mid$ $Zero+, V_{out}, -V_{in}$	3-4e	$N-1 < \frac{V_{out}}{V_{in}} < \infty$	$K_A = \frac{1}{2}$ $K_{Bin} = \frac{-1}{2}, 0 < K_{Bout} < \frac{1}{2}$	$V_{in}, V_{out} + V_{in}$
$V_{in}, Zero- \mid$ $V_{in}, V_{out}, Zero-$	3-4g	$N < \frac{V_{out}}{V_{in}} < \infty$	$K_A = \frac{1}{2}$ $\frac{-1}{2} < K_{Bin} < 0, 0 < K_{Bout} < \frac{1}{2}$	V_{in}, V_{out}

3.3 Results from Prototype PT-based Converter

We validate these switching sequences and associated analyses with an experimental prototype PT-based converter that implements the $V_{in}, Zero+, Zero- \mid V_{out}, V_{in}$ non-isolated switching sequence using a commercially available PT [9]. We chose to implement a non-isolated converter because non-isolated PTs are more easily obtainable given their prevalent use for CCFL backlights. Fig. 3-5 shows the circuit topology implemented by the prototype. This switching sequence requires topology 3-4b in Fig. 3-4, which can be realized with only two active switches (for the switch node at the input port since the input port is regulating). Table 3.5 shows the specifications of the parts used in the prototype. The parameters of the PT used in the prototype are given by Table 3.6. The actual circuit board populated with these components is shown in Fig. 3-6. Full schematics, board layouts, and a bill of materials

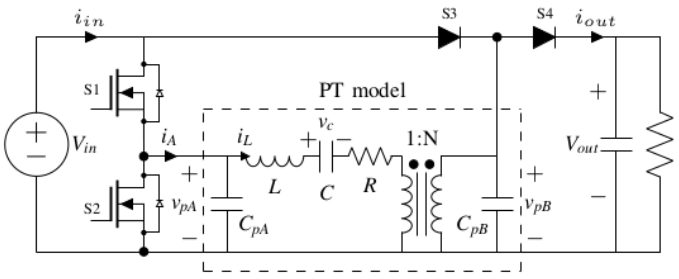

Figure 3-5: Circuit Topology for Prototype: This circuit is identical to topology 3-4b in Fig. 3-4 except switches $S3$ and $S4$ are replaced with diodes [9].

are provided in Jessica Boles' thesis [6].

Parameter	Manufacturer-Provided [1]	On-Board Measurement
C_{pA}	960 pF	1.6 nF (with switches)
C_{pB}	8 pF	83 pF (with diodes)
L	59 mH	44 mH
C	60 pF	72 pF
R	24 Ω	27 Ω
N	6	6 (assumed)

Table 3.5: Parameters of PT in prototype

Component	Part
PT	STEMiNC SMSTF50P2S6
Active Switch	EPC 2012C GaN FET
Schottky Diode	Genesic Semiconductor GB01SLT06-214
Gate Driver	Texas Instruments UCC27611

Table 3.6: Prototype Parts List

3.3.1 Waveforms

Fig. 3-7 shows the prototype's v_{pA} and v_{pB} waveforms operating at constant $V_{in} = 180\,\text{V}$, constant $P_{out} = 900\,\text{mW}$, and various V_{out} values. These waveforms show that the prototype operates as expected and goes through the states of the switching sequence as described in Section 2.2. They also demonstrate how the switching sequence regulates for different voltage gains. For higher V_{out} and voltage gains, the length of the $Zero+$ stage in the input sub-sequence shortens until it disappears when $V_{out} = 360\,\text{V}$. This is equivalent to going through the range of K_A for this switching

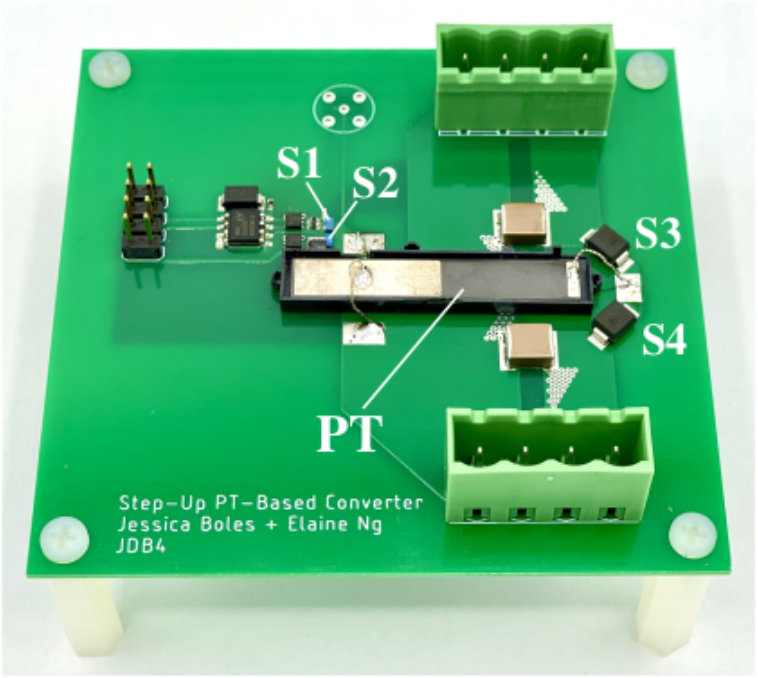

Figure 3-6: Prototype circuit board for the $V_{in}, Zero+, Zero-|V_{out}, V_{in}$ and its corresponding topology 3-4b

sequence, $0 < K_A < \frac{1}{2}$. When $K_A \approx \frac{1}{2}$, the input port spends the most time in its V_{in} stage, the only stage where charge is being transferred from the source through the input port, compared to the time spent in the other stages.

3.3.2 ZVS and Efficiency

Fig. 3-8 plots the whole-converter efficiency vs. $\frac{V_{out}}{V_{in}}$ at a constant $V_{in} = 60\,\text{V}$ for various power levels. The efficiency drops quickly as voltage gain decreases, which is a behavior expected for this switching sequence since the input port is used for regulation.

Fig. 3-9 similarly shows the whole-converter efficiency as a function of $\frac{V_{out}}{V_{in}}$ but at a constant $V_{out} = 360\,\text{V}$. This plot shows that the converter reaches a peak efficiency of around 90%, which is much higher than many of the efficiencies of other PT-based converters in literature as shown in Table 1.1 in Section 1.1. This converter is also able to regulate voltage at a high $\frac{V_{out}}{V_{in}}$ ratio without the efficiency penalties for large conversion ratios seen in PR-based converters. The relatively flat efficiency

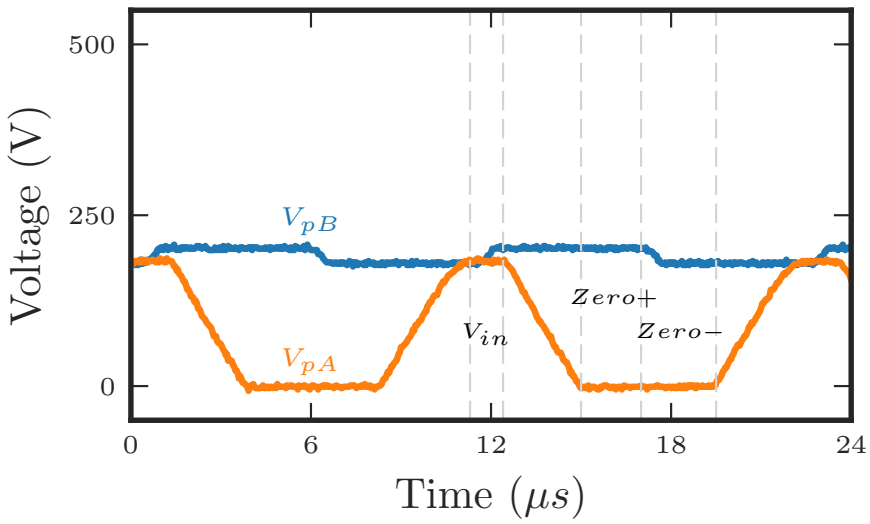

(a) $V_{in} = 180\,\mathrm{V}, V_{out} = 200\,\mathrm{V}, P_{out} = 900\,\mathrm{mW}$

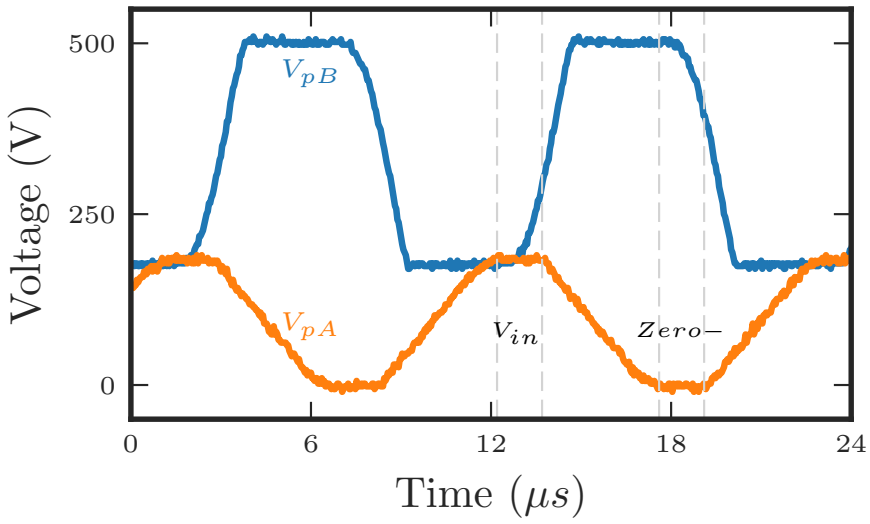

(b) $V_{in} = 180\,\mathrm{V}, V_{out} = 500\,\mathrm{V}, P_{out} = 900\,\mathrm{mW}$

Figure 3-7: Time-domain experimental waveforms for the prototype.

curves with respect to V_{in} is predicted by the amplitude of resonance not changing for constant V_{out} for this switching sequence.

Fig. 3-9 also shows that the converter loses ZVS at low $\frac{V_{out}}{V_{in}}$ ratios as indicated by the ZVS boundary calculated using the analysis in Section 2.6. This suggests that the efficiency is limited to around 90% because of the ZVS boundary determined by the parameters of the off-the-shelf PT used in the prototype (STEMiNC SMSTF50P2S6),

which is not optimized for this use case. The rest of this thesis explores how to combine the benefits of the circuit-level design strategies used to design this prototype and component-level optimization to improve the efficiency capabilities of PT components beyond 90%.

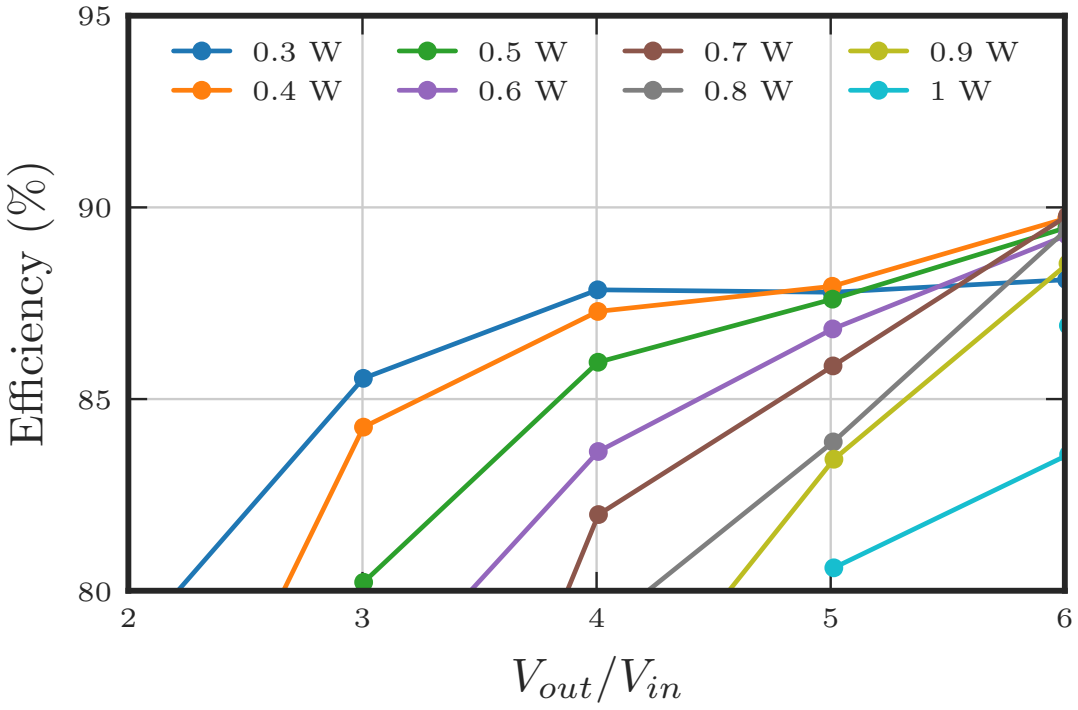

Figure 3-8: Whole-converter efficiency vs. $\frac{V_{out}}{V_{in}}$ for constant $V_{in} = 60\,\text{V}$ at various power levels (marked).

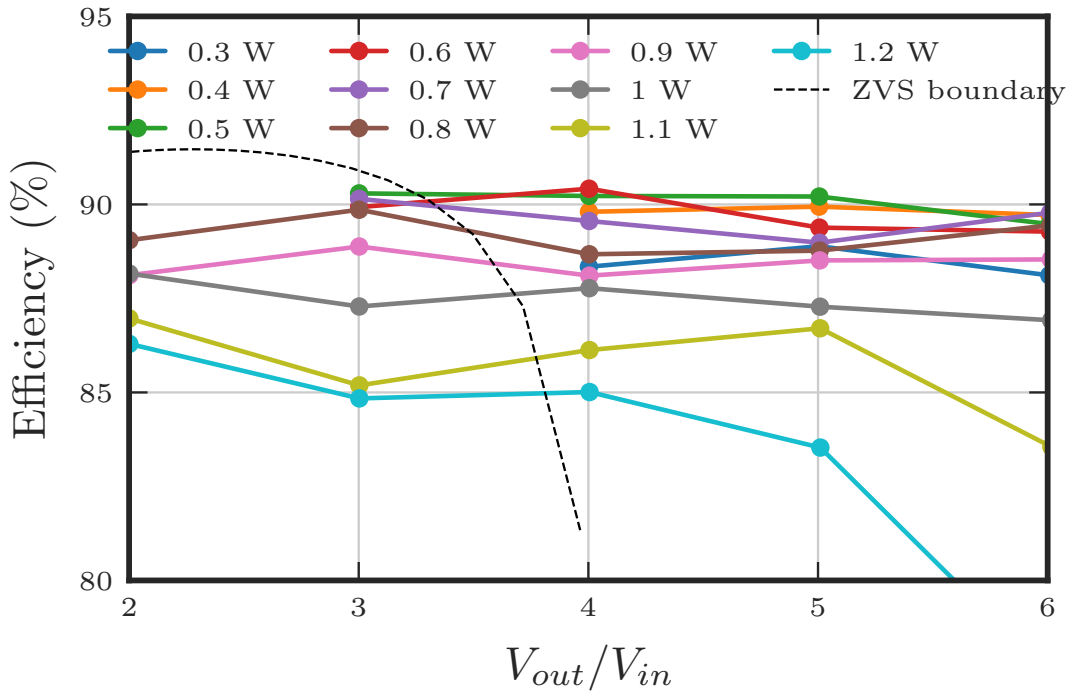

Figure 3-9: Whole-converter efficiency vs. $\frac{V_{out}}{V_{in}}$ for constant $V_{out} = 360\,\text{V}$ at various power levels (marked). ZVS boundary is calculated using the method shown in Section 2.6.

Chapter 4

PT Model

u	Mechanical Displacement (m)
T	Mechanical Stress (N/m^2)
S	Mechanical Strain
E	Electric Field Strength (N/m)
D	Electric Flux Density (C/m^2)

Table 4.1: Material State Definitions from [8]

Q_m	Mechanical Quality Factor
k	Electromechanical Coupling Factor
v_a	Acoustic Velocity (m/s)
ρ	Mass Density (kg/m^3)
ϵ	Dielectric Constant (F/m)
s	Compliance Constant (m^2/N)
d	Piezoelectric Charge Constant (C/N)
c	Elastic Modulus (N/m^2)
e	Piezoelectric Strain Modulus (C/m^2)
σ	Poisson's Ratio

Table 4.2: Material Property Definitions from [8]

In the following chapters, we explore improved possibilities for designing a PT component for power conversion. In order to do that, we first must understand how to relate the parameters of the reduced Mason model to the geometric and material properties of a PT. In this chapter, we present a promising PT structure, $k_{33} - k_{33}$ and derive its reduced Mason model from its constitutive relations.

4.1 Explanation of PT Structures

A PT can be thought of as two PRs mechanically coupled to each other. The Mason model of an individual PR includes an electric circuit analog for the mechanical motion of the acoustic wave traveling through the PR. Thus, the Mason model of each PR can

Mode	s^E	d	ϵ^T	v_a	k	Diagram
Length Extensional (side electrodes)	s^E_{11}	d_{31}	ϵ^T_{33}	$\sqrt{\frac{1}{\rho s^E_{11}}}$	$k_{31} = \frac{d_{31}}{\sqrt{s^E_{11}\epsilon^T_{33}}}$	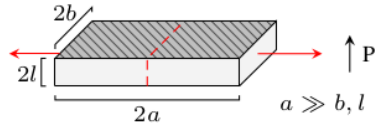
Length Extensional (end electrodes)	s^E_{33}	d_{33}	ϵ^T_{33}	$\sqrt{\frac{1}{\rho s^D_{33}}}$	$k_{33} = \frac{d_{33}}{\sqrt{s^E_{33}\epsilon^T_{33}}}$	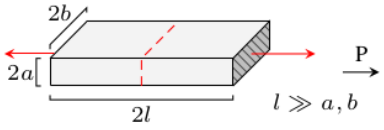
Thickness Shear (side electrodes)	s^E_{55}	d_{15}	ϵ^T_{11}	$\sqrt{\frac{1}{\rho s^D_{55}}}$	$k_{15} = \frac{d_{15}}{\sqrt{s^E_{55}\epsilon^T_{11}}}$	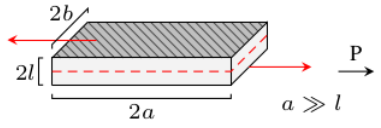
Thickness Shear (end electrodes)	s^E_{55}	d_{15}	ϵ^T_{11}	$\sqrt{\frac{1}{\rho s^E_{55}}}$	$k_{15} = \frac{d_{15}}{\sqrt{s^E_{55}\epsilon^T_{11}}}$	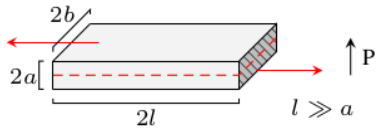
Thickness Extensional (side electrodes)	**	**	**	$\sqrt{\frac{c^D_{33}}{\rho}}$	$k_t = \frac{e_{33}}{\sqrt{c^D_{33}\epsilon^S_{33}}}$	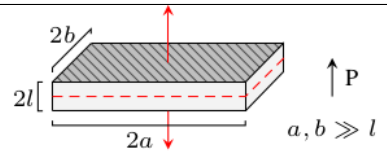
Contour Extensional	s^E_{11}	d_{31}	ϵ^T_{33}	$\sqrt{\frac{1}{\rho s^E_{11}(1-\sigma^2)}}$	$k_p = \sqrt{\frac{2k^2_{31}}{1-\sigma}}$	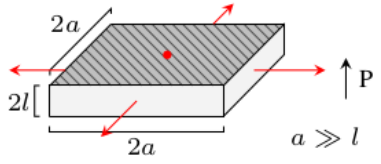
Radial	s^E_{11}	d_{31}	ϵ^T_{33}	$\sqrt{\frac{1}{\rho s^E_{11}(1-\sigma^2)}}$	$k_p = \sqrt{\frac{2k^2_{31}}{1-\sigma}}$	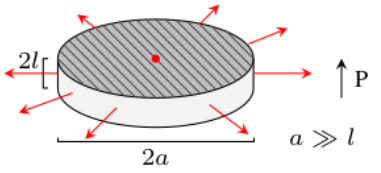

Figure 4-1: Summary of PR vibration modes and their corresponding material parameters from [8]. Diagrams show electrodes denoted by shaded areas, mechanical displacement direction(s) with red arrows, and polarization direction denoted by P. **Thickness extensional mode is commonly represented by e_{33}, c^E_{33}, and ϵ^S_{33} [8].

be derived separately starting with a piezoelectric material's constitutive relations, which relate the material states through the properties shown in Table 4.1. These individual PR models can then be connected to each other using boundary conditions to create the Mason model for the entire PT.

PRs can come in a variety of shapes, electrode configurations, and vibration modes. Fig. 4-1 shows some common PR vibration modes. These modes are often labeled by their corresponding electromechanical coupling factor (k). Like many of the material properties shown in Table 4.2, k is a function of tensor components. We will use indices to designate tensor components. For example, the indices of k_{31} indicate that the k_{31} mode PR is polarized along the x_3 direction but its mechanical displacement is along the x_1 direction. Other parameters like the compliance constant (s) have superscripts (e.g. s^E, s^D, etc.) to denote the material state that is held constant during their measurement [8].

Fig. 4-2 shows the Rosen-type PT structure, which is one of the most widely available PT structures today[1]. This structure consists of a k_{31} mode PR that excites a k_{33} mode PR that is mechanically cascaded with it. The Rosen-type is an example of a non-isolated PT, consisting of three terminals. Fig. 4-3 shows the $k_{33} - k_{33}$ PT structure, where both PRs vibrate in the k_{33} mode. There is an assumed insulation layer in between the two PRs for galvanic isolation, which allows the structure to have four terminals. The mechanical properties of this electrical insulation layer are neglected, but it is assumed that mechanical traveling waves can traverse the insulation layer unimpeded. (It is also noted that one can have a non-isolated 3-terminal device in which such an insulation layer is not required.) We focus on this $k_{33} - k_{33}$ structure for the remainder of this theoretical study.

[8] derives figures of merit to evaluate different PR materials and vibration modes for power conversion. Table 4.3 summarizes the efficiency figure of merit and energy handling density figure of merit for the modes studied for an example piezoelectric material. One can think of "energy handling density" as volumetric power density normalized to frequency. This table shows that the k_{31} mode PR has much lower

[1]The commericial PT used in the prototype discussed in Chapter 3 is a Rosen type PT.

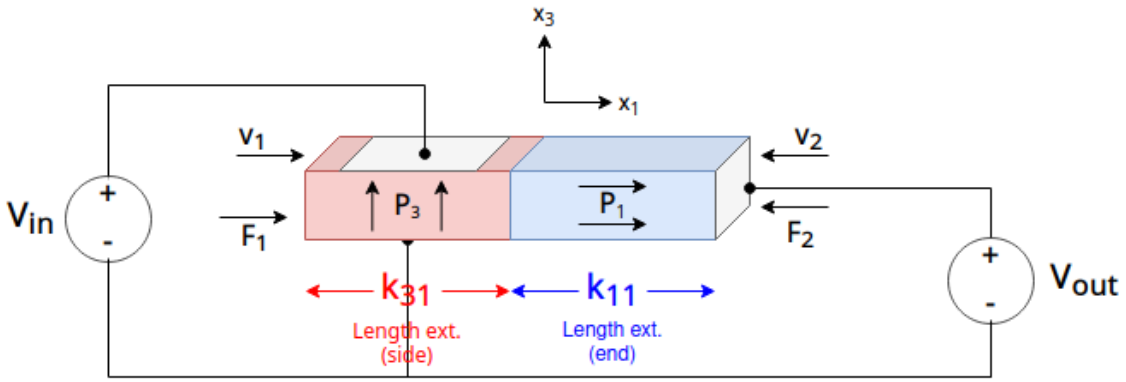

Figure 4-2: Diagram of the Rosen-type PT structure. This structure consists of a length extensional (side) or k_{31} mode PR in-series with a length extensional (end) or k_{11} mode PR. Note because the polarization and mechanical displacement are in the x_1 direction for the right PR in this structure, the right PR is labeled as k_{11}. The length extensional (end) PR is typically labeled with k_{33} by itself.

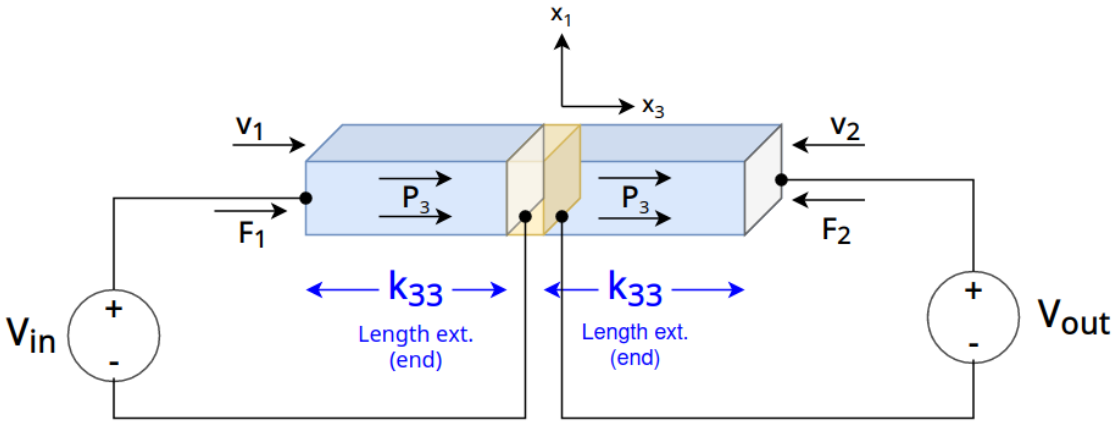

Figure 4-3: Diagram of the $k_{33} - k_{33}$ PT structure. Both PRs are length extensional (end). An insulation layer (yellow) is inserted in between the two PRs, so there can be four electrodes. This insulation layer only provides galvanic insulation. It is assumed that acoustic waves can travel through the insulation layer and electrode layers unimpeded.

Mode	Efficiency Figure of Merit	Energy Handling Density Figure of Merit
Length Extensional (side)	63.4	377
Length Extensional (end)	345	1930
Thickness Shear (side)	303	2740
Thickness Shear (end)	338	3210
Thickness Extensional	138	631
Contour Extensional	229	13200
Radial	223	15600

Table 4.3: PR vibration mode comparison from [8]. Figures of merit were calculated for hard PZT (PIC181) [8].

efficiency and energy handling density figures of merit than the other modes. We choose the $k_{33} - k_{33}$ PT structure to keep the same simplicity of the Rosen-type but replace its k_{31} mode PR with a k_{33} mode PR to improve the efficiency and power density capabilities of the entire structure.

4.2 Mason Model for k_{33} PR

To derive the Mason model for the $k_{33} - k_{33}$ PT, we first derive the Mason model for a single k_{33} PR. Then we connect the Mason models of the PRs together via their boundary conditions at the interface [38]. In this section, we derive the Mason model for the k_{33} PR shown in Fig. 4-4.

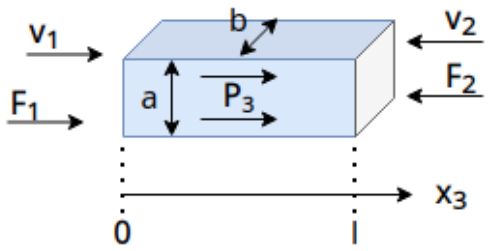

Figure 4-4: Diagram of k_{33} PR: This PR has height a, width b, and length l. The ends of the PR are free from force.

PRs are governed by coupled equations relating mechanical strain (**S**), mechanical stress (**T**), electric field strength (**E**), and electric flux density (**D**). We use boldface to indicate quantities that are **phasors**. These coupled constitutive equations can be written in many forms, but for the k_{33} mode, it is convenient to begin with the strain-voltage form:

$$\begin{aligned} \boldsymbol{S_3} &= s_{33}^D \boldsymbol{T_3} + g_{33} \boldsymbol{D_3} \\ \boldsymbol{E_3} &= -g_{33} \boldsymbol{T_3} + \beta_{33} \boldsymbol{D_3} \end{aligned} \tag{4.1}$$

where g_{33}, β_{33}, and s_{33}^D are also material properties related to the properties shown in

Table 4.2 by:

$$\begin{aligned} g_{33} &= \frac{d_{33}}{\epsilon_{33}^T} \\ \beta_{33}^T &= \frac{1}{\epsilon_{33}^T} \\ s_{33}^D &= s_{33}^E(1 - k_{33}^2) \end{aligned} \tag{4.2}$$

(4.1) assumes stress, strain, and $\boldsymbol{E}$ are one-dimensional. The total stress applied to the cross-sectional area ab to displace the PR's length by Δx_3 is $\Sigma \boldsymbol{T_3} = \frac{\partial \boldsymbol{T_3}}{\partial x_3}\Delta x_3$. We can express the net force as a function of stress as: $\Sigma \boldsymbol{F} = \Sigma \boldsymbol{T_3} \times \text{Area} = \Big(\frac{\partial \boldsymbol{T_3}}{\partial x_3}\Delta x_3\Big)(ab)$. Using Newton's first law, we can derive the following equation of motion for the PR:

$$\begin{aligned} \Sigma \boldsymbol{F} &= m\frac{\partial^2 \boldsymbol{u_3}}{\partial t^2} \\ \Big(\frac{\partial \boldsymbol{T_3}}{\partial x_3}\Delta x_3\Big)(ab) &= (\rho ab \Delta x_3)\Big(\frac{\partial^2 \boldsymbol{u_3}}{\partial t^2}\Big) \end{aligned} \tag{4.3}$$

Solving for $\boldsymbol{T_3}$ in (4.1) yields:

$$\boldsymbol{T_3} = \frac{1}{s_{33}^D}\boldsymbol{S_3} - \frac{g_{33}}{s_{33}^D}\boldsymbol{D_3} \tag{4.4}$$

Substituting (4.4) into (4.3) results in the following wave equation where we have used the dot notation to denote derivatives with respect to the time variable t:

$$\ddot{\boldsymbol{u_3}} = \frac{1}{\rho s_{33}^D}\frac{\partial^2 \boldsymbol{S_3}}{\partial x_3^2} \tag{4.5}$$

(4.5) has solutions of the form:

$$\boldsymbol{u_3} = \boldsymbol{B_1}\sin \kappa x_3 + \boldsymbol{B_2}\cos \kappa x_3 \tag{4.6}$$

where $\kappa = \frac{\omega}{v_a}$ and $v_a = \frac{1}{\sqrt{\rho s_{33}^D}}$.

$\boldsymbol{B_1}$ and $\boldsymbol{B_2}$ in (4.6) can be calculated using the following boundary conditions regarding the forces and velocities at the ends of the PR:

1. $\boldsymbol{F_1} = -(\boldsymbol{T_3}|_{x_3=0})(ab)$

2. $\boldsymbol{F_2} = -(\boldsymbol{T_3}|_{x_3=l})(ab)$

3. $\boldsymbol{v_1} = \frac{\partial \boldsymbol{u_3}}{\partial t}|_{x_3=0}$

4. $\boldsymbol{v_2} = -\frac{\partial \boldsymbol{u_3}}{\partial t}|_{x_3=l}$

Substituting (4.4) for $\boldsymbol{T_3}$ and (4.6) for $\boldsymbol{u_3}$ and simplifying yields these simplified boundary conditions:

1. $\boldsymbol{F_1} = -\frac{ab}{s_{33}^D}(\boldsymbol{B_1}\kappa - g_{33}\boldsymbol{D_3})$

2. $\boldsymbol{F_2} = -\frac{ab}{s_{33}^D}(\boldsymbol{B_1}\kappa\cos\kappa l - \boldsymbol{B_2}\kappa\sin\kappa l - g_{33}\boldsymbol{D_3})$

3. $\boldsymbol{v_1} = j\omega\boldsymbol{B_2}$

4. $\boldsymbol{v_2} = -j\omega(\boldsymbol{B_1}\sin\kappa l + \boldsymbol{B_2}\cos\kappa l)$

Combining boundary conditions 3 and 4 gives the following expression for $\boldsymbol{B_1}$:

$$\boldsymbol{B_1} = -\frac{1}{j\omega}\Big(\frac{\boldsymbol{v_1}}{\tan\kappa l} + \frac{\boldsymbol{v_2}}{\sin\kappa l}\Big) \tag{4.7}$$

Rearranging boundary condition 3 also gives the following expression for $\boldsymbol{B_2}$:

$$\boldsymbol{B_2} = \frac{\boldsymbol{v_1}}{j\omega} \tag{4.8}$$

Now we analyze the electric port of the PR. Let $\boldsymbol{I}$ be the current into the left electrode in Fig. 4-4 and $\boldsymbol{V}$ be the voltage across the entire PR.

We calculate $\boldsymbol{I}$ from taking the time derivative of the charge calculated using Gauss's Law.

$$\begin{aligned} \boldsymbol{I} &= \frac{\partial}{\partial t}\oint \boldsymbol{D_3}\cdot dA \\ &= j\omega\boldsymbol{D_3}ab \end{aligned} \tag{4.9}$$

And we can calculate the voltage by integrating the electric field. Note electric field $\boldsymbol{E_3}$ is in the opposite direction of $\boldsymbol{P_3}$ shown in Fig. 4-4.

$$\begin{aligned}\boldsymbol{V} &= -\int_0^l (-\boldsymbol{E_3}) \cdot dx_3 \\ &= \int_0^l (-g_{33}\boldsymbol{T_3} + \beta_{33}^T \boldsymbol{D_3}) dx_3 \\ &= \int_0^l \Big(- g_{33}\Big(\frac{1}{s_{33}^D}\Big)(\boldsymbol{S_3} - g_{33}\boldsymbol{D_3}) + \beta_{33}^T \boldsymbol{D_3}\Big) dx_3\end{aligned} \tag{4.10}$$

where we substituted (4.4) for $\boldsymbol{T_3}$ from the second-to-last line to the last line.

$$\begin{aligned}\boldsymbol{V} &= -\frac{g_{33}}{s_{33}^D}\int_0^l \boldsymbol{S_3} dx_3 + \int_0^l \Big(\beta_{33}^T + \frac{g_{33}^2}{s_{33}^D}\Big)\boldsymbol{D_3} dx_3 \\ &= -\frac{g_{33}}{s_{33}^D}(\boldsymbol{u_3}|_{x_3=l} - \boldsymbol{u_3}|_{x_3=0}) + \Big(\beta_{33}^T + \frac{g_{33}^2}{s_{33}^D}\Big) l\boldsymbol{D_3}\end{aligned} \tag{4.11}$$

where we used the definition that $\boldsymbol{S_3} = \frac{\partial \boldsymbol{u_3}}{\partial x_3}$. Rearranging (4.9) for $\boldsymbol{D_3}$ yields:

$$\boldsymbol{D_3} = \frac{\boldsymbol{I}}{j\omega ab} \tag{4.12}$$

$\boldsymbol{u_3}|_{x_3=l} - \boldsymbol{u_3}|_{x_3=0}$ can be simplified by substituting (4.6) for $\boldsymbol{u_3}$, (4.7) for $\boldsymbol{B_1}$, and (4.8) for $\boldsymbol{B_2}$.

$$\boldsymbol{u_3}|_{x_3=l} - \boldsymbol{u_3}|_{x_3=0} = \frac{1}{j\omega}(\boldsymbol{v_1} + \boldsymbol{v_2}) \tag{4.13}$$

Now we substitute (4.12) and (4.13) into (4.11) and simplify:

$$\boldsymbol{V} = \frac{g_{33}}{s_{33}^D}\Big(\frac{1}{j\omega}\Big)(\boldsymbol{v_1} + \boldsymbol{v_2}) + l\Big(\beta_{33}^T + \frac{g_{33}^2}{s_{33}^D}\Big)\Big(\frac{\boldsymbol{I}}{j\omega ab}\Big) \tag{4.14}$$

This expression can be further simplified by using the following material property relations:

$$\begin{aligned} g_{33} &= \frac{d_{33}}{\epsilon_{33}^T} \\ \beta_{33}^T + \frac{g_{33}^2}{s_{33}^D} &= \frac{1}{\epsilon_{33}^T(1 - k_{33}^2)}\end{aligned} \tag{4.15}$$

which yields the following final expression for $\boldsymbol{V}$:

$$\boldsymbol{V} = \frac{1}{j\omega C_0}\psi(\boldsymbol{v_1} + \boldsymbol{v_2}) + \frac{1}{j\omega C_0}\boldsymbol{I} \tag{4.16}$$

where

$$C_0 = \frac{\epsilon_{33}^T(1 - k_{33}^2)ab}{l} \tag{4.17}$$

and

$$\psi = \frac{d_{33}}{s_{33}^E}\Big(\frac{ab}{l}\Big) \tag{4.18}$$

Using boundary condition 1, (4.7) for $\boldsymbol{B_1}$, and (4.12) for $\boldsymbol{D_3}$ we can express $\boldsymbol{F_1}$ in terms of $\boldsymbol{v_1}$, $\boldsymbol{v_2}$ and $\boldsymbol{I}$.

$$\boldsymbol{F_1} = \frac{Z_0}{j\tan\kappa L}\boldsymbol{v_1} + \frac{Z_0}{j\sin\kappa L}\boldsymbol{v_2} + \frac{1}{j\omega C_0}\psi\boldsymbol{I} \tag{4.19}$$

where

$$Z_0 = \frac{\kappa ab}{s_{33}^D\omega} \tag{4.20}$$

We solve for $\frac{1}{j\omega C_0}$ in (4.16):

$$\frac{1}{j\omega C_0}\boldsymbol{I} = \boldsymbol{V} - \frac{1}{j\omega C_0}\psi(\boldsymbol{v_1} + \boldsymbol{v_2}) \tag{4.21}$$

Substituting (4.21) and the trigonometry identity: $\frac{1}{\tan\kappa l} - \frac{1}{\sin\kappa l} = \tan\frac{\kappa l}{2}$ yields this final expression for $\boldsymbol{F_1}$:

$$\boldsymbol{F_1} = Z_1\boldsymbol{v_1} + Z_2(\boldsymbol{v_1} + \boldsymbol{v_2}) + \psi\Big(\boldsymbol{V} - \frac{1}{j\omega C_0}\psi(\boldsymbol{v_1} + \boldsymbol{v_2})\Big) \tag{4.22}$$

where

$$\begin{aligned} Z_1 &= jZ_0\tan\frac{\kappa l}{2} \\ Z_2 &= \frac{Z_0}{j\sin\kappa l} \end{aligned} \tag{4.23}$$

Through similar analysis, $\boldsymbol{F_2}$ can be expressed as:

$$\boldsymbol{F_2} = Z_1\boldsymbol{v_2} + Z_2(\boldsymbol{v_1} + \boldsymbol{v_2}) + \psi\Big(\boldsymbol{V} - \frac{1}{j\omega C_0}\psi(\boldsymbol{v_1} + \boldsymbol{v_2})\Big) \tag{4.24}$$

We can now rewrite (4.22), (4.24), and (4.16) by converting between the mechanical domain variables $(\boldsymbol{F_1}, \boldsymbol{F_2}, \boldsymbol{v_1}, \boldsymbol{v_2})$ to the electrical domain variables $(\boldsymbol{E_1}, \boldsymbol{E_2}, \boldsymbol{I_1}, \boldsymbol{I_2})$ to arrive at the following system of KVL equations:

$$\begin{cases} \boldsymbol{E_1} = Z_1\boldsymbol{I_1} + Z_2(\boldsymbol{I_1} + \boldsymbol{I_2}) + \psi\Big(\boldsymbol{V} - \frac{1}{j\omega C_0}\psi(\boldsymbol{I_1} + \boldsymbol{I_2})\Big) \\ \boldsymbol{E_2} = Z_1\boldsymbol{I_2} + Z_2(\boldsymbol{I_1} + \boldsymbol{I_2}) + \psi\Big(\boldsymbol{V} - \frac{1}{j\omega C_0}\psi(\boldsymbol{I_1} + \boldsymbol{I_2})\Big) \\ \boldsymbol{V} = \frac{1}{j\omega C_0}\psi(\boldsymbol{I_1} + \boldsymbol{I_2}) + \frac{1}{j\omega C_0}\boldsymbol{I} \end{cases} \tag{4.25}$$

The first two equations of (4.25) can be represented by a Y-shaped impedance network (also sometimes called a "T network" or a "star network"). To account for the voltage drop of $-\frac{1}{j\omega C_0}\psi(\boldsymbol{I_1} + \boldsymbol{I_2})$ in these two equations, an extra negative-valued capacitance $-C_0$ or inductor with inductance $L_0 = \frac{1}{\omega^2 C_0}$ is needed between C_0 and the ideal transformer. Finally, Fig. 4-5 shows the full Mason model circuit for the k_{33} PR given by (4.25). The derived Mason model parameters for the k_{33} PR are shown in Table 4.4.

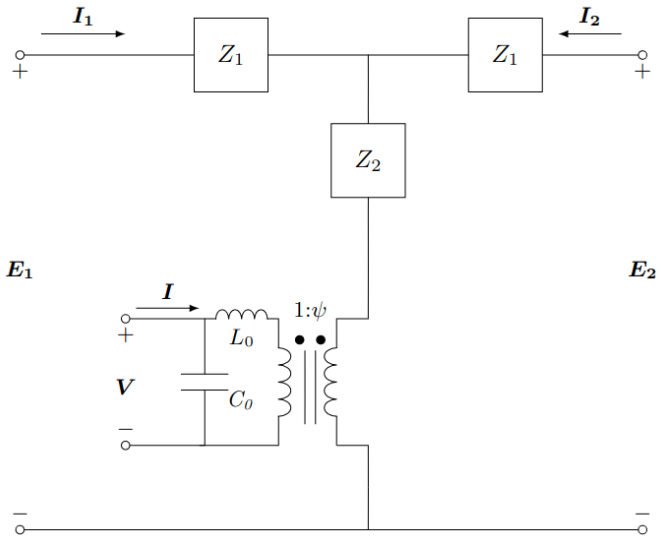

Figure 4-5: Mason model for the k_{33} PR. Circuit parameters shown are given by Table 4.4.

Parameter	Expression
Z_1	$jZ_0 \tan \frac{\kappa l}{2}$
Z_2	$\frac{Z_0}{j \sin \kappa l}$
Z_0	$\frac{\kappa ab}{s_{33}^D \omega}$
C_0	$\frac{\epsilon_{33}^T (1-k_{33}^2) ab}{l}$
L_0	$\frac{1}{\omega^2 C_0}$
ψ	$\frac{d_{33}}{s_{33}^E} \left(\frac{ab}{l} \right)$

Table 4.4: Parameters for the Mason Model of the k_{33} PR

4.3 Mason Model for $k_{33} - k_{33}$ PT

To derive the Mason model for the full $k_{33} - k_{33}$ PT structure, we can relate the Mason models of two individual k_{33} PRs with boundary conditions [38]. For the purposes of this theoretical study, we assume the insulation layer in between the two PRs takes up zero width. We also assume perfect mechanical coupling between the two PRs at this interface, neglecting any effects of the electrodes. After applying boundary conditions, we will simplify the circuit to reach the final reduced Mason model for this structure.

4.3.1 Connecting PR Mason Models Together

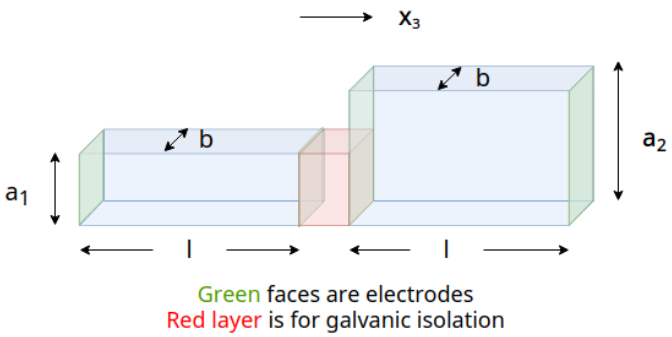

Figure 4-6: Diagram for $k_{33} - k_{33}$ PT with labeled dimensions: The two PRs have identical dimensions except their heights

For this study, we assume that all of the dimensions for both PRs are the same **except their heights** (a_1 and a_2) as shown in Fig. 4-6. To derive the Mason model

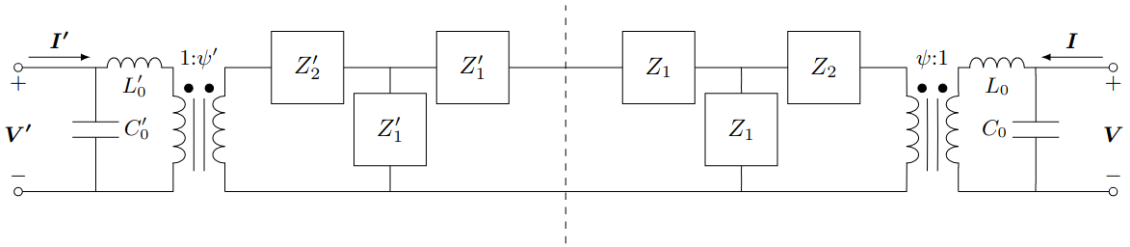

Figure 4-7: This circuit is the result of joining the Mason models of two k_{33} PRs with the boundary conditions listed in Section 4.3.1. Circuit parameters are given by Table 4.5.

Left PR		Right PR	
Z_1'	$jZ_0' \tan \frac{\kappa l}{2}$	Z_1	$jZ_0 \tan \frac{\kappa l}{2}$
Z_2'	$\frac{Z_0'}{j \sin \kappa l}$	Z_2	$\frac{Z_0}{j \sin \kappa l}$
Z_0'	$\frac{\kappa a_1 b}{s_{33}^D \omega}$	Z_0	$\frac{\kappa a_2 b}{s_{33}^D \omega}$
C_0'	$\frac{\epsilon_{33}^T (1-k_{33}^2) a_1 b}{l}$	C_0	$\frac{\epsilon_{33}^T (1-k_{33}^2) a_2 b}{l}$
L_0'	$\frac{1}{\omega^2 C_0'}$	L_0	$\frac{1}{\omega^2 C_0}$
ψ'	$\frac{d_{33}}{s_{33}^E}\left(\frac{a_1 b}{l}\right)$	ψ	$\frac{d_{33}}{s_{33}^E}\left(\frac{a_2 b}{l}\right)$

Table 4.5: Parameters for the circuit shown in Figure 4-7.

for the $k_{33} - k_{33}$ PT, we connect the individual Mason model of each k_{33} PR with boundary conditions at the interface. These boundary conditions include:

1. **Continuity of velocities at the interface**: $-\boldsymbol{I_2'} = \boldsymbol{I_1}$ at $x_3 = 0$

2. **Continuity of forces at the interface**: $\boldsymbol{E_2'} = \boldsymbol{E_1}$ at $x_3 = 0$

3. **Ends are free from force**: $\boldsymbol{E_1'} = \boldsymbol{E_2} = 0$

These boundary conditions lead to the circuit shown in Fig. 4-7. Primed variables ($\prime$) indicate parameters for the left PR in the $k_{33} - k_{33}$ PT structure shown in Fig. 4-6. Unprimed variables indicate parameters for the right PR. While this circuit is technically the Mason model for the full PT structure, we can take steps to simplify this circuit into the standard reduced Mason model form.

First we transform the Δ-network formed by impedances Z_1', Z_1', Z_1, and Z_1 into

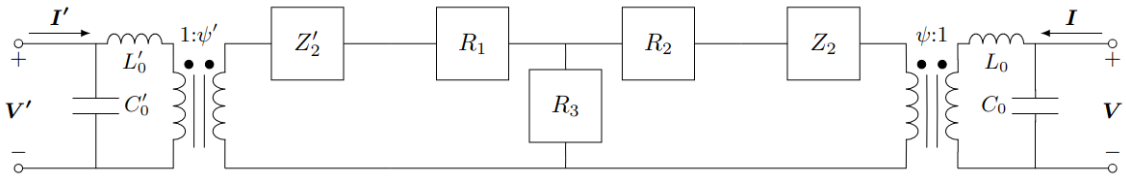

Figure 4-8: This circuit is the result of performing a Δ to Y transformation described in Section 4.3.1 to the circuit shown in Fig. 4-7. Expressions for R_1, R_2, and R_3 are given by (4.26).

a Y-network as shown in Fig. 4-8 where

$$\begin{aligned} R_1 &= \frac{Z_1'(Z_1' + Z_1)}{Z_1' + (Z_1' + Z_1) + Z_1} = \frac{j}{2} Z_0' \tan\frac{\kappa l}{2} \\ R_2 &= \frac{Z_1(Z_1' + Z_1)}{Z_1' + (Z_1' + Z_1) + Z_1} = \frac{j}{2} Z_0 \tan\frac{\kappa l}{2} \\ R_3 &= \frac{Z_1' Z_1}{2(Z_1' + Z_1)} = \frac{j Z_0' Z_0 \tan\frac{\kappa l}{2}}{2(Z_0' + Z_0)} \end{aligned} \tag{4.26}$$

This network can be further simplified by combining impedances that are in series as:

$$\begin{aligned} Z_2' + R_1 &= \frac{Z_0'}{2j \tan\frac{\kappa l}{2}} \\ Z_2 + R_2 &= \frac{Z_0}{2j \tan\frac{\kappa l}{2}} \\ R_3 &= \frac{j Z_0' Z_0 \tan\frac{\kappa l}{2}}{2(Z_0' + Z_0)} \end{aligned} \tag{4.27}$$

The reduced Mason model for a PT is an equivalent circuit that represents the PT when it is operating near anti-resonance, or when $\kappa l = \pi$. κ is the wave number (in rad/m). For convenience, we normalize κ to geometry such that: $\kappa = \frac{\kappa_0}{l}$. κ_0 is the geometry-normalized wave number (in rad) [8]. Under this condition, $\tan\frac{\kappa l}{2} = \tan\frac{\kappa_0}{2} \to \infty$ and $R_3 \to \infty$. Since R_3 is effectively an open circuit, we can ignore its contribution and the impedance network between the transformers simplifies to a single impedance $Z(\kappa_0)$ as shown by Fig. 4-9:

$$Z(\kappa_0) = \frac{Z_0' + Z_0}{2j \tan\frac{\kappa_0}{2}} \tag{4.28}$$

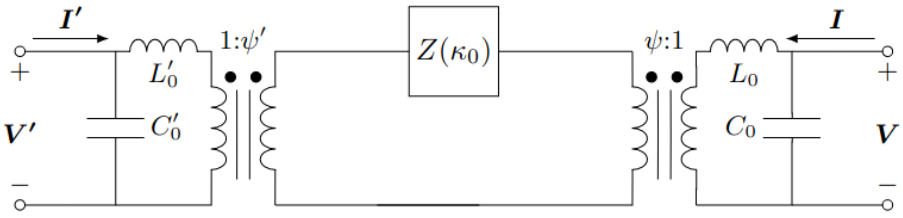

Figure 4-9: The impedance network can now be expressed as a single impedance $Z(\kappa_0)$.

4.3.2 Simplifying the Circuit by Taylor Expansion

We can now Taylor expand $Z(\kappa_0)$ around $\kappa_0 = \pi$. At this point, the lower order derivatives of $Z(\kappa_0)$ are as follows:

$$\begin{aligned} Z(\kappa_0) &\to 0 \\ \frac{\partial Z}{\partial \kappa_0} &= \frac{j\pi(Z_0' + Z_0)}{4} \\ \frac{\partial^2 Z}{\partial \omega^2} &\to 0 \end{aligned} \tag{4.29}$$

The Taylor expansion for $Z(\kappa_0)$ is then:

$$Z(\kappa_0) = \frac{j(Z_0' + Z_0)}{4}(\kappa_0 - \pi) \tag{4.30}$$

We can compare the expression given by (4.30) with the impedance of a series LC network given by:

$$\begin{aligned} Z_{LC}(\kappa_0) &= j\omega L_m + \frac{1}{j\omega C_m} \\ &= j\sqrt{\frac{L_m}{C_m}}\left(\frac{\omega}{\omega_0} - \frac{\omega_0}{\omega}\right) \\ &= j\sqrt{\frac{L_m}{C_m}}\left(\frac{\kappa_0}{\pi} - \frac{\pi}{\kappa_0}\right) \end{aligned} \tag{4.31}$$

where from the first line to the second line, we have used the fact that $\omega_0 = \frac{1}{\sqrt{L_m C_m}}$. To get to the last line, we substituted $\omega = \frac{\kappa_0 v_a}{l}$ and $\omega_0 = \frac{\pi v_a}{l}$. If we similarly Taylor

expand (4.31) around $\kappa_0 = \pi$, we derive:

$$Z_{LC}(\kappa_0) = \frac{2j\omega_0 L_m}{\pi}(\kappa_0 - \pi) \tag{4.32}$$

By matching terms in (4.30) and (4.32), we can conclude that the impedance network represented by $Z(\kappa_0)$ can be replaced with a series RLC network with parameters given by:

$$\begin{aligned} L_m &= \frac{\pi(Z_0' + Z_0)}{8\omega_0} \\ C_m &= \frac{1}{\omega_0^2 L_m} \\ R_m &= \frac{\omega_0 L_m}{Q_m} \end{aligned} \tag{4.33}$$

where Q_m is the quality factor of one of the PRs.

4.3.3 Reflection to Derive the Reduced Mason Model

The last step to derive the reduced Mason model is to reflect the series RLC network across one of the transformers. Fig. 4-10 shows the Mason model before this reflection where the circuit parameters are given by (4.33). We can choose to have the final transformer either on the input side or on the output side, without loss of generality, we select to derive the output-side transformer Mason model. This requires reflecting the network across the $(1 : \psi')$ transformer. Thus the reflected circuit parameters can be obtained by (4.34). The two transformers can also be combined into one $(1 : N)$ transformer where N is also given by (4.34). Appendix A.1 shows how to derive the reduced Mason model with the input-side transformer.

$$\begin{aligned} R_{reflected} &= \frac{R_m}{\psi'^2} \\ L_{reflected} &= L_0' + \frac{L_m}{\psi'^2} + L_0\Big(\frac{\psi}{\psi'}\Big)^2 \\ C_{reflected} &= C_m\psi'^2 \\ N &= \frac{\psi'}{\psi} \end{aligned} \tag{4.34}$$

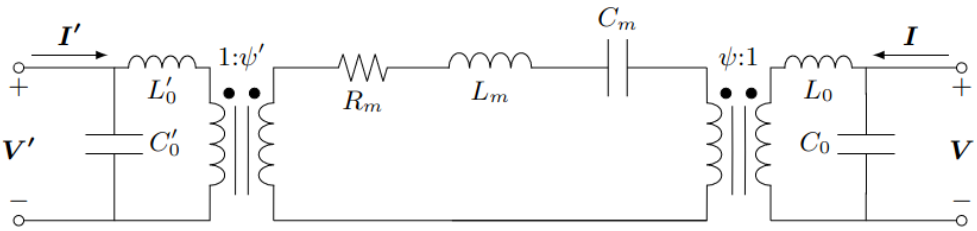

Figure 4-10: This is the circuit where $Z(\kappa_0)$ in Fig. 4-9 is replaced by a series RLC network with parameters given by (4.33).

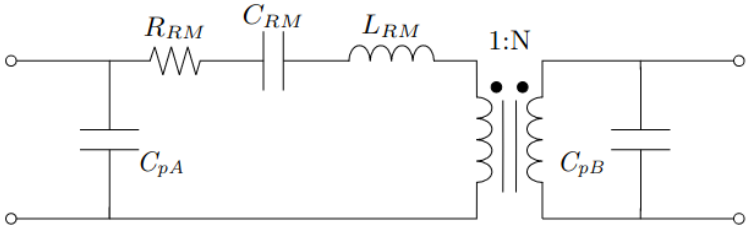

Figure 4-11: Final reduced Mason model for the $k_{33} - k_{33}$ PT with parameters given by (4.35).

This yields the final reduced Mason model for the $k_{33} - k_{33}$ PT. Fig. 4-11 shows this circuit with the labels for the parameters that we will use in the remainder of this thesis ($R_{RM} = R_{reflected}$, $L_{RM} = L_{reflected}$, $C_{RM} = C_{reflected}$, $C_{pA} = C_0'$, and $C_{pB} = C_0$). The parameters of Fig. 4-11 are given by (4.35).

$$
\begin{aligned}
R_{RM} &= \frac{\pi}{8Q_m v_a k_{33}^2 \epsilon_{33}^T (1-k_{33}^2)}(a_1+a_2)\left(\frac{l^2}{a_1^2 b}\right) \\
L_{RM} &= \left(\frac{1}{\omega_0^2}\right)\left(\frac{l}{\epsilon_{33}^T(1-k_{33}^2)a_1 b}\right)\left(1+\frac{a_2}{a_1}+\left(\frac{1}{8k_{33}^2}\right)(a_1+a_2)\left(\frac{\pi^2}{a_1}\right)\right) \\
C_{RM} &= \frac{8k_{33}^2\epsilon_{33}^T(1-k_{33}^2)}{\pi^2}\left(\frac{1}{a_1+a_2}\right)\left(\frac{a_1^2 b}{l}\right) \\
C_{pA} &= \left(\frac{a_1 b}{l}\right)\epsilon_{33}^T(1-k_{33}^2) \\
C_{pB} &= \left(\frac{a_2 b}{l}\right)\epsilon_{33}^T(1-k_{33}^2) \\
N &= \frac{a_1}{a_2}
\end{aligned}
\tag{4.35}
$$

If we assume the heights of the PRs are related by a scaling factor α such that $a_2 = \alpha a_1$, which we do to derive the geometry conditions in Chapters 5-7, (4.35) can

be simplified to:

$$
\begin{aligned}
R_{RM} &= \frac{\pi(1+\alpha)l}{8Q_m v_a k_{33}^2 C_{pA}} \\
L_{RM} &= \frac{1+\alpha}{\omega_0^2 C_{pA}}\left(1+\frac{\pi^2}{8k_{33}^2}\right) \\
C_{RM} &= \frac{8k_{33}^2 C_{pA}}{\pi^2(1+\alpha)} \\
C_{pA} &= \left(\frac{a_1 b}{l}\right)\epsilon_{33}^T(1-k_{33}^2) \\
C_{pB} &= \alpha C_{pA} \\
N &= \frac{1}{\alpha}
\end{aligned}
\tag{4.36}
$$

Chapter 5

Maximum Efficiency Geometry Condition

With the Mason model of the $k_{33}-k_{33}$ PT, we can now express its electrical behavior in terms of geometry and material properties. At a high level, our process for designing a PT is to constrain its geometric dimensions (α, b, and l) for high efficiency and high power density while maintaining ZVS[1]. Optimizing with respect to these geometry terms yields independent conditions for each of these dimensions as shown in Fig. 5-1. In the following chapters, we derive these geometry conditions for the $k_{33}-k_{33}$ PT structure. In this chapter, we focus on efficiency, or (equivalently) minimum loss ratio.

5.1 Separating Geometry and Material Terms in Circuit Model Parameters

All of the geometry conditions presented in this thesis depend on the Mason model circuit parameters derived in Chapter 4. Since our goal is to constrain geometry, it is helpful to rewrite some of these parameters with their geometry and material terms separated (i.e. explicitly in the form of "f(geometry terms)g(material terms)" where

[1]This approach of constraining the geometry of the PT by optimizing metrics like efficiency is similar to the design strategies for designing PRs discussed in [8].

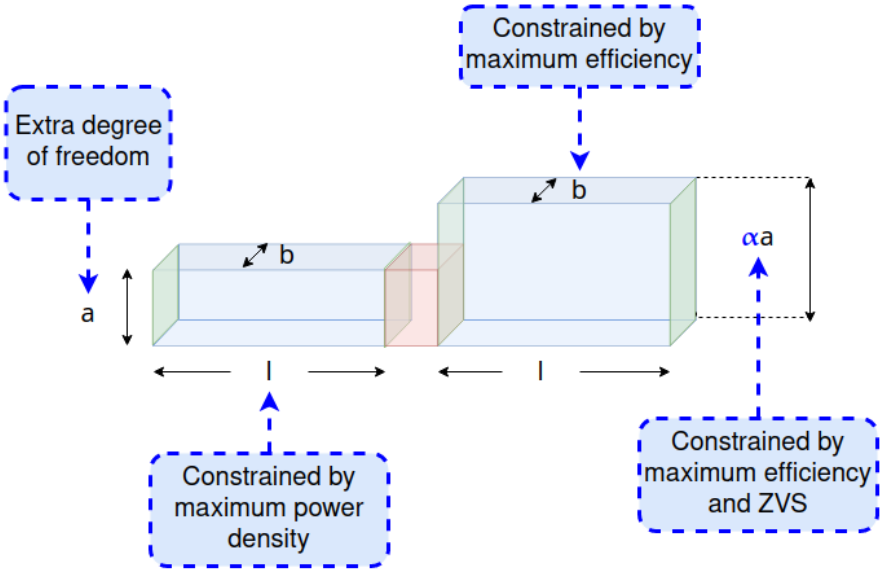

Figure 5-1: Dimensions α, b, and l are constrained to optimize metrics indicated. a is left as an extra degree of freedom.

f and g are separate functions). For further convenience, we assume the heights of the two PRs to be related by a scaling factor α such that:

$$\begin{aligned} a_2 &= \alpha a_1 \\ a_1 &= a \end{aligned} \tag{5.1}$$

as shown by Fig. 5-1.

5.1.1 Resistance R_{RM}

From Chapter 4, the resistance in reduced Mason model is:

$$R_{RM} = \frac{\pi}{8Q_m v_a k_{33}^2 \epsilon_{33}^T (1-k_{33}^2)} (a_1 + a_2)\left(\frac{l^2}{a_1^2 b}\right) \tag{5.2}$$

By substituting $a_1 = a$ and $a_2 = \alpha a$, this simplifies to:

$$R_{RM} = \frac{\pi}{8Q_m v_a k_{33}^2 \epsilon_{33}^T (1-k_{33}^2)} (1+\alpha)\left(\frac{l^2}{ab}\right) \tag{5.3}$$

where red terms are material terms and blue terms are geometry terms. For simplicity later in the optimization, we encapsulate some of these terms into a material-dependent R_0 and geometry factor G.

$$R_{RM} = R_0(1+\alpha)\left(\frac{1}{G}\right) \tag{5.4}$$

where:

$$R_0 = \frac{\pi}{8Q_m v_a k_{33}^2 \epsilon_{33}^T (1-k_{33}^2)} \tag{5.5}$$

and

$$G = \frac{ab}{l^2} \tag{5.6}$$

5.1.2 Frequency-Capacitance Product B

Many metrics like efficiency depend on a frequency-capacitance product quantity, e.g. fC_{pA} or fC_{pB}. From Chapter 4, the terminal capacitances C_{pA} and C_{pB} are:

$$\begin{aligned} C_{pA} &= \left(\frac{a_1 b}{l}\right)\epsilon_{33}^T(1-k_{33}^2) \\ C_{pB} &= \alpha C_{pA} \end{aligned} \tag{5.7}$$

We use the following naming convention:

$$\begin{aligned} B &= fC_{pA} \\ \alpha B &= fC_{pB} \end{aligned} \tag{5.8}$$

Substituting (5.7) and $f = \frac{\kappa_0 v_a}{2\pi l}$ into (5.8) yields:

$$B = \left(\frac{\kappa_0 v_a}{2\pi l}\right)\left(\frac{\epsilon_{33}^T(1-k_{33}^2)ab}{l}\right) \tag{5.9}$$

We similarly separate geometry and material terms:

$$B = \left(\frac{\kappa_0 v_a \epsilon_{33}^T(1-k_{33}^2)}{2\pi}\right)\left(\frac{ab}{l^2}\right) \tag{5.10}$$

By allowing,

$$B_0 = \frac{\kappa_0 v_a \epsilon_{33}^T (1 - k_{33}^2)}{2\pi} \tag{5.11}$$

B can be expressed as:

$$B = B_0 G \tag{5.12}$$

5.2 Minimum Loss Ratio and Geometry Condition

In Chapter 2, we estimate PT efficiency and loss ratio $\frac{P_{loss}}{P_{out}}$ using the amplitude of resonance I_L. Since peak efficiency corresponds to minimum loss ratio, we derive the maximum efficiency by minimizing the loss ratio. We can choose to do this analysis with respect to the input port or the output port. For correspondence with the design shown in Chapter 8, the analysis presented in this chapter is with respect to the input port. Please refer to Appendix A.2 for the derivation with respect to the output port.

We calculate the amplitude of resonance with respect to the input port $I_{L,in}$ as:

$$I_{L,in} = \pi\left(\frac{P_{out}}{2K_A V_{in}} + BV_{ppA}\right) \tag{5.13}$$

The loss ratio with respect to the input port is then:

$$\begin{aligned} \frac{P_{loss}}{P_{out}}\Big|_{in} &= \frac{\frac{1}{2} I_{L,in}^2 R}{P_{out}} \\ &= \frac{\pi^2 R_0 (1+\alpha)}{2P_{out}} \left(\frac{P_{out}^2}{4K_A^2 V_{in}^2} \left(\frac{1}{G}\right) + \frac{P_{out} V_{ppA} B_0}{K_A V_{in}} + G B_0^2 V_{ppA}^2 \right) \end{aligned} \tag{5.14}$$

Minimizing (5.14) with respect to the geometry factor G yields the following minimum loss ratio:

$$\frac{P_{loss}}{P_{out}}\Big|_{in,min} = \frac{\pi^2 (1+\alpha) R_0 B_0 V_{ppA}}{K_A V_{in}} \tag{5.15}$$

which is reached when G is constrained to be:

$$G_{in,efficiency} = \frac{P_{out}}{2K_A B_0 V_{in} V_{ppA}} \tag{5.16}$$

For many switching sequences (including the sequence selected for the design in Chapter 8), V_{ppA} is proportional to V_{in}. In these cases, (5.15) only depends on material properties and α for these switching sequences. Note the form of this expression is very close to the expression for the minimum loss ratio for PRs except for the factor of $(1+\alpha)$, which comes from the geometry of the $k_{33}-k_{33}$ PT structure. Using (2.10) from Chapter 2, we also derive an expression for peak PT efficiency:

$$\eta_{peak} = \left(1 + \frac{\pi^2(1+\alpha)R_0 B_0 V_{ppA}}{K_A V_{in}}\right)^{-1} \tag{5.17}$$

Chapter 6

Geometry Condition for Zero Voltage Switching (ZVS)

6.1 ZVS Geometry Condition

Chapter 2 introduces a strategy for modeling a given switching sequence's ZVS region. For an isolated switching sequence, the ZVS region is constrained by:

$$\frac{P_{out}}{fK_AV_{in}} + 2C_{pA}V_{ppA} = N\Big(\frac{P_{out}}{fK_BV_{out}} + 2C_{pB}V_{ppB}\Big) \tag{6.1}$$

Substituting $f = \frac{\kappa_0 v_a}{2\pi l}$ and the expressions for the reduced Mason model parameters into this equation yields:

$$\frac{P_{out}}{K_AV_{in}}\Big(\frac{2\pi}{\kappa_0 v_a}\Big) + 2\epsilon_{33}^T(1-k_{33}^2)GV_{ppA} = \frac{1}{\alpha}\left(\frac{P_{out}}{K_BV_{out}}\Big(\frac{2\pi}{\kappa_0 v_a}\Big) + 2\epsilon_{33}^T(1-k_{33}^2)\alpha GV_{ppB}\right) \tag{6.2}$$

where $G = \frac{ab}{l^2}$, the same geometry factor in the minimum loss ratio optimization. This equation can be solved for G:

$$G = \frac{\pi P_{out,min}}{\kappa_0 v_a \epsilon_{33}^T(1-k_{33}^2)(V_{ppB}-V_{ppA})}\Big(\frac{1}{K_AV_{in}} - \frac{1}{\alpha K_BV_{out}}\Big) \tag{6.3}$$

This can be simplified by using $B_0 = \frac{\kappa_0 v_a \epsilon_{33}^T (1-k_{33}^2)}{2\pi}$ to derive a geometry condition for maintaining ZVS:

$$G_{ZVS} = \frac{\pi P_{out,min}}{2B_0(V_{ppB} - V_{ppA})}\Big(\frac{1}{K_A V_{in}} - \frac{1}{\alpha K_B V_{out}}\Big) \tag{6.4}$$

Note that we have replaced P_{out} with $P_{out,min}$ in the ZVS geometry condition. $P_{out,min}$ is the minimum power level for which the switching sequence can maintain ZVS. If a lower power level than $P_{out,min}$ is needed, one may use a different switching sequence.

6.2 Constraining α with ZVS and Maximum Efficiency Conditions

The ZVS geometry condition depends on both α and G, but by substituting the maximum efficiency geometry condition, G is eliminated. Setting (5.16) = (6.4), we derive an expression for α. If maximum efficiency occurs at the desired minimum power level (i.e. $P_{out,min} = P_{out}$), α is:

$$\alpha = \frac{K_A V_{in} V_{ppA}}{K_B V_{out}(2V_{ppA} - V_{ppB})} \tag{6.5}$$

For other power levels, a designer may choose a minimum power level that occurs at $P_{out,min} = \chi P_{out}$. α in this more general case is:

$$\alpha = \frac{\chi K_A V_{in} V_{ppA}}{K_B V_{out}(V_{ppA}(\chi + 1) - V_{ppB})} \tag{6.6}$$

Chapter 7

Maximum Power Density Geometry Condition

In this chapter, we derive the last of the geometry conditions for optimizing power density. For our design process, we focus on deriving maximum energy handling density, which can be calculated by dividing the PT's power density capability by its frequency. We utilize the amplitude of resonance I_L to calculate the PT's power handling capability. As in the case of minimum loss ratio, this power density maximum derivation can be done with respect to either the input port or output port. Here, we present the derivation with respect to the input port. Appendix A.3 shows the derivation with respect to the output port.

7.1 Maximum I_L Derivation for the k_{33} PR

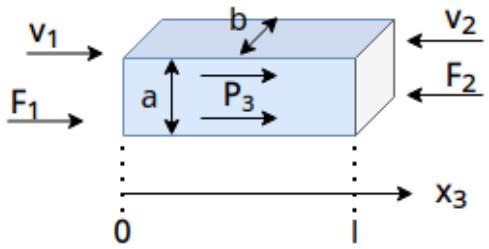

Figure 7-1: Diagram of k_{33} PR repeated for convenience

Since we seek to maximize power density with respect to geometry, we first separate the geometry and material terms in I_L. Fig. 7-1 repeats the diagram of a k_{33} PR for convenience. To calculate I_L through this PR, we first calculate charge on the left electrode and then differentiate with respect to time.

There are two ways to calculate this charge. For the first way, we simply use Gauss' Law to analyze the charge of a surface that encloses just the left electrode. Integrating $\boldsymbol{D_3}$ over the left electrode's area gives the charge on the electrode:

$$Q_{left} = \oint \boldsymbol{D_3} \cdot dA \tag{7.1}$$

We can substitute a constitutive piezoelectric equation, $\boldsymbol{D_3} = \frac{d_{33}}{s_{33}^E}\frac{\partial \boldsymbol{u_3}}{\partial x_3} + \epsilon_{33}^T(1-k_{33}^2)\boldsymbol{E_3}$. (7.1) is then:

$$Q_{left} = A\Big(\frac{d_{33}}{s_{33}^E}\frac{\partial \boldsymbol{u_3}}{\partial x_3} + \epsilon_{33}^T(1-k_{33}^2)\boldsymbol{E_3}\Big) \tag{7.2}$$

where $A = ab$ is the cross-sectional area of the PR. By Gauss' Law, $\boldsymbol{D_3}$ is constant along the direction of propagation of the acoustic wave, x_3. Thus Q_{left} given by (7.2) is constant with respect to x_3 and can be thought of as the linear charge density along x_3. By this definition, $Q_{left} = \frac{Q_{PT}}{l}$, where Q_{PT} can be calculated by integrating Q_{left} from over the entire length of the PR. Using such a roundabout way of calculating Q_{left} from Q_{PT} allows us to relate Q_{left} to the voltage across the PR (v_p). Q_{PT} is:

$$Q_{PT} = \int_0^l A\Big(\frac{d_{33}}{s_{33}^E}\frac{\partial \boldsymbol{u_3}}{\partial x_3} + \epsilon_{33}^T(1-k_{33}^2)\boldsymbol{E_3}\Big)dx_3 \tag{7.3}$$

Substituting $\boldsymbol{E_3} = -\frac{\partial \boldsymbol{V}}{\partial x_3}$ yields:

$$\begin{aligned} Q_{PT} &= \int_0^l A\Big(\frac{d_{33}}{s_{33}^E}\frac{\partial \boldsymbol{u_3}}{\partial x_3}dx_3 + \int_0^l \epsilon_{33}^T(1-k_{33}^2)\boldsymbol{E_3}\Big)dx_3 \\ &= A\frac{d_{33}}{s_{33}^E}\Big(\boldsymbol{u_3}(l) - \boldsymbol{u_3}(0)\Big) + \epsilon_{33}^T(1-k_{33}^2)A\Big(\boldsymbol{V}(l) - \boldsymbol{V}(0)\Big) \end{aligned} \tag{7.4}$$

From Section 4.2, $\boldsymbol{u_3}$ can be written in the form $\boldsymbol{B}\sin\kappa x_3$ where $\boldsymbol{B}$ is a phasor coefficient solved through boundary conditions. Thus, $\boldsymbol{u_3}(l) - \boldsymbol{u_3}(0)$ simplifies to just $\boldsymbol{u_3}(l)$. $\boldsymbol{V}(l) - \boldsymbol{V}(0)$ is the difference in electric potential between the ends of the PR,

or equivalently the voltage across the PR v_p. As a result,

$$Q_{left} = \frac{A}{l}\frac{d_{33}}{s_{33}^E}\boldsymbol{u_3}(l) + \frac{A}{l}\epsilon_{33}^T(1-k_{33}^2)v_p \tag{7.5}$$

Differentiating (7.5) with respect to t results in the following equation for the current through the left electrode:

$$i_{left} = j\omega\frac{A}{l}\frac{d_{33}}{s_{33}^E}\boldsymbol{u_3}(l) + \frac{A}{l}\epsilon_{33}^T(1-k_{33}^2)\frac{dv_p}{dt} \tag{7.6}$$

The amplitude of resonance I_L is the magnitude of the first term in (7.6). Thus, the maximum I_L is:

$$\begin{aligned} I_L &= j(\kappa v_a)\frac{A}{l}\frac{d_{33}}{s_{33}^E}\boldsymbol{B}\sin\kappa l \\ &= j(\kappa v_a)\frac{A}{l}\frac{d_{33}}{s_{33}^E}\boldsymbol{B}\sin\kappa_0 \end{aligned} \tag{7.7}$$

The only geometry terms in the above equation are $\frac{A}{l}$. Thus, the amplitude of resonance I_L can be written as:

$$I_L = \frac{A}{l}I_{Lmax0} = \frac{ab}{l}I_{Lmax0} \tag{7.8}$$

where I_{Lmax0} is the geometry-normalized I_L and encapsulates all the material terms in (7.7).

PZT PRs operating in the k_{33} mode are limited by a loss density [6]. This is also the case for the PT in the experimental prototype of Chapter 3. Thus, we derive a limit for I_L based on loss density. We define $H_{max} = \frac{P_{loss}}{\text{Area}}$ as the loss density with respect to the **input port**. Since most of the heat is assumed to be extracted through the electrode, Area $= ab$ is the cross-sectional area of the input PR[1].

$$H_{max} = \frac{P_{loss}}{ab} = \frac{1}{2}\frac{I_L^2 R}{ab} \tag{7.9}$$

[1]If the loss density with respect to the output port is specified, the cross-sectional area of the output PR is needed or Area $= \alpha ab$.

If we substitute (5.4) for R into (7.9) and extract geometry terms from I_L:

$$\begin{aligned} H_{max} &= \frac{1}{2}\Big(\frac{I_{Lmax0}ab}{l}\Big)^2 R_0(1+\alpha)\Big(\frac{1}{G}\Big)\Big(\frac{1}{ab}\Big) \\ &= \frac{1}{2}I_{Lmax0}^2 R_0(1+\alpha) \end{aligned} \tag{7.10}$$

I_{Lmax0} can be calculated by solving the above equation as:

$$I_{Lmax0} = \sqrt{\frac{2}{R_0(1+\alpha)}H_{max}} \tag{7.11}$$

To use this expression, the designer must choose a reasonable maximum loss density for H_{max} depending on the intended thermal design.

7.2 Power Handling Capability P_{out}

With the geometry and material terms separated in I_L, we can use I_L to calculate P_{out}. The amplitude of resonance with respect to the input port is:

$$I_{L,in} = \pi\Big(\frac{P_{out}}{2K_A V_{in}} + BV_{ppA}\Big) \tag{7.12}$$

Solving for P_{out} in the above equation yields:

$$P_{out} = 2K_A V_{in}\Big(\frac{I_{L,in}}{\pi} - BV_{ppA}\Big) \tag{7.13}$$

We can write out the geometry and material terms in $I_{L,in}$ and B and simplify:

$$P_{out} = 2K_A V_{in}\Big(\frac{ab}{l}\Big)\Big(\frac{I_{Lmax0}}{\pi} - \frac{B_0 V_{ppA}}{l}\Big) \tag{7.14}$$

7.3 Maximum Energy Handling Density and Geometry Condition

The total volume of the $k_{33} - k_{33}$ PT is:

$$\begin{aligned} \text{vol} &= a_1 bl + a_2 bl \\ &= bl(a + \alpha a) \\ &= abl(1 + \frac{1}{N}) \\ &= \frac{abl(N+1)}{N} \end{aligned} \tag{7.15}$$

Energy handling density is defined to be $\frac{E_{out}}{\text{vol}} = \frac{P_{out}}{\text{vol} \cdot f}$. Substituting (7.14) and (7.15) into this definition:

$$\begin{aligned} \frac{E_{out}}{\text{vol}} &= \frac{2K_A V_{in} N}{l^2(1+N)} \Big(\frac{I_{Lmax0}}{\pi} - \frac{B_0 V_{ppA}}{l} \Big) \Big(\frac{2\pi l}{\kappa_0 v_a} \Big) \\ &= \frac{4K_A V_{in} \pi N}{\kappa_0 v_a (1+N)} \Big(\frac{I_{Lmax0}}{\pi l} - \frac{B_0 V_{ppA}}{l^2} \Big) \end{aligned} \tag{7.16}$$

We can maximize (7.16) with respect to l to obtain a geometry condition for maximum energy handling density. The maximum energy handling density is:

$$\frac{E_{out}}{\text{vol}}\Big|_{max} = \frac{K_A V_{in} I_{Lmax0}^2 N}{\pi \kappa_0 v_a B_0 V_{ppA} (1+N)} \tag{7.17}$$

which occurs at an optimized length:

$$l_{power} = \frac{2\pi B_0 V_{ppA}}{I_{Lmax0}} \tag{7.18}$$

where I_{Lmax0} is given by (7.11).

Chapter 8

Full Theoretical Design of a PT-Based Converter

In this chapter, we design a high-efficiency, high-power-density PT-based converter by combining the high-efficiency, isolated switching sequence $V_{in}, -V_{in}|V_{out}, -V_{out}, Zero+$ and a PT component designed with the geometry conditions derived in Chapters 5, 6, and 7. A Python script for designing a PT for this switching sequence is provided in Appendix A.4. This design is validated through simulations in MATLAB and LTspice[1].

[1]These MATLAB and LTspice simulations were written by my advisor Jessica Boles and are included in her thesis [6].

8.1 Summary of Switching Sequence Parameters and Geometry Conditions

The parameters of the chosen $V_{in}, -V_{in}|V_{out}, -V_{out}, Zero+$ switching sequence are repeated here for convenience:

$$\begin{aligned} V_{ppA} &= 2V_{in} \\ V_{ppB} &= 2V_{out} \\ K_A &= 1 \\ \frac{1}{2} &< K_B < 1 \end{aligned} \tag{8.1}$$

We also repeat the geometry conditions derived in the previous chapters for convenience:

- Efficiency Condition: $G_{in,efficiency} = \frac{P_{out}}{2K_A B_0 V_{in} V_{ppA}}$
- ZVS Condition: $G_{ZVS} = \frac{\pi P_{out,min}}{2B_0(V_{ppB}-V_{ppA})}\left(\frac{1}{K_A V_{in}} - \frac{1}{\alpha K_B V_{out}}\right)$
- Power Density Condition: $l_{power} = \frac{2\pi B_0 V_{ppA}}{I_{Lmax0}}$

where:

$$\begin{aligned} P_{out,min} &= \chi P_{out} \\ B_0 &= \frac{\kappa_0 v_a \epsilon_{33}^T (1-k_{33}^2)}{2\pi} \\ I_{Lmax0} &= \sqrt{\frac{2}{R_0(1+\alpha)}} H_{max} \\ R_0 &= \frac{\pi}{8 Q_m v_a k_{33}^2 \epsilon_{33}^T (1-k_{33}^2)} \end{aligned} \tag{8.2}$$

α can be constrained by both the efficiency and ZVS conditions as explained in Chapter 6 using the following equation.

$$\alpha = \frac{\chi K_A V_{in} V_{ppA}}{K_B V_{out}(V_{ppA}(\chi+1) - V_{ppB})} \tag{8.3}$$

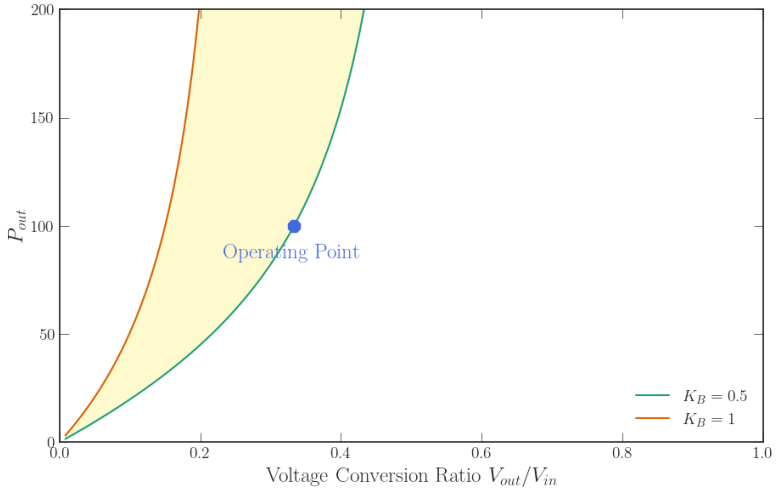

Figure 8-1: ZVS Region of a PT Designed with $\chi = 1$ and Minimum K_B. The nominal operating point ($\frac{V_{out}}{V_{in}} = 0.33, P_{out} = 100\,\text{W}$) is labeled and occurs at the minimum K_B boundary.

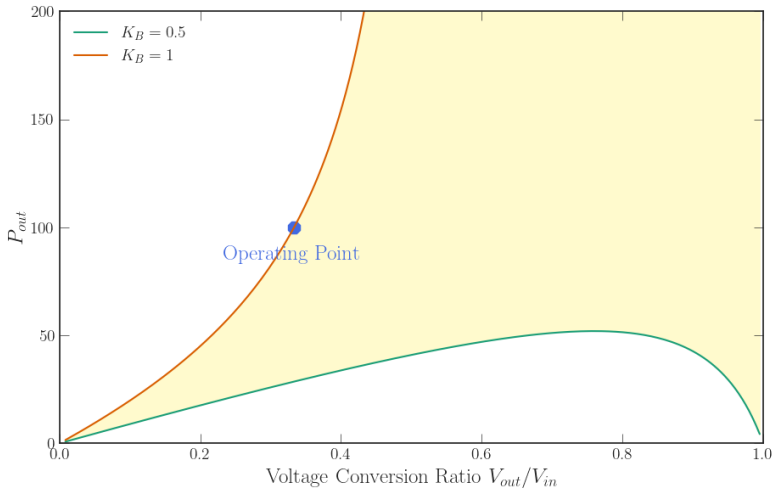

Figure 8-2: ZVS Region of a PT Designed with $\chi = 1$ and Maximum K_B: The nominal operating point ($\frac{V_{out}}{V_{in}} = 0.33, P_{out} = 100\,\text{W}$) is labeled and occurs at the maximum K_B boundary.

8.2 PT Design Process

For this design process, a designer may assume a switching sequence and either a nominal operating point $(V_{in}, V_{out}, P_{out})$ or range of operating points. First, α is selected using (8.3). For simplicity, a designer may choose to design for ZVS with a single operating point ($\chi = 1$). In this case, we suggest selecting K_B to be near the middle of the K_B range for the switching sequence to ensure ZVS using a single

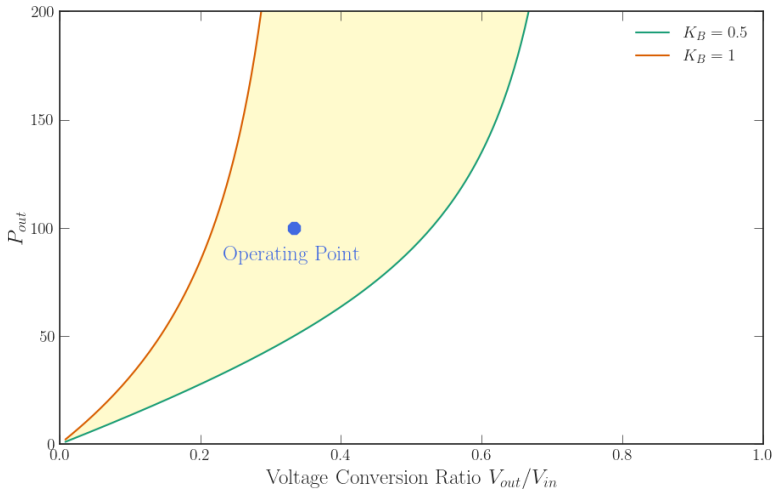

Figure 8-3: ZVS Region of a PT Designed with $\chi = \frac{1}{2}$ and Minimum K_B: The nominal operating point ($\frac{V_{out}}{V_{in}} = 0.33, P_{out} = 100\,\text{W}$) is labeled and occurs inside the ZVS region. Assuming the same operating voltages, ZVS is lost at a power level $\chi P_{out} = 50\,\text{W}$.

operating point. If an extremum of the range is used, the nominal operating point would occur at one of the ZVS boundaries as shown by Fig. 8-1 and Fig. 8-2. $\chi \neq 1$ allows greater freedom in designing for more operating points to occur inside the ZVS region as shown by Fig. 8-3.

Once an α is selected, l can be constrained using the power density geometry condition. To use this geometry condition, an estimated loss limit with respect to the input port H_{max} is assumed. If the loss limit with respect to the output port $H_{max,out}$ is specified, then $H_{max} = \frac{H_{max,out}}{\alpha}$.

There is an extra degree of freedom in the scaling between a and b. For this theoretical study, we choose $a = b$ and calculate a using the maximum efficiency geometry condition.

$$\begin{aligned} G &= \frac{P_{out}}{2K_A B_0 V_{in} V_{ppA}} \\ a &= \frac{l}{\sqrt{G}} \end{aligned} \tag{8.4}$$

Thus, all the dimensions of the PT are determined.

Parameter	Value
ρ	$7600\,\mathrm{kg/m^3}$
ϵ_{33}^T	$12.17\,\mathrm{nF/m}$
s_{33}^D	$8.533\,\mu\mathrm{m^2/N}$
v_a	$3.927\,\mathrm{km/s}$
k_{33}	0.68
Q_m	1400

Table 8.1: Assumed PT Material Properties (APC 841) [2]

Parameter	Value
α	2.25
l	$8.00\,\mathrm{mm}$
a, b	$9.30\,\mathrm{mm}$
C_{pA}	$707\,\mathrm{pF}$
C_{pB}	$1.59\,\mathrm{nF}$
L_{RM}	$70.9\,\mu\mathrm{H}$
C_{RM}	$81.6\,\mathrm{pF}$
R_{RM}	$0.57\,\Omega$

Table 8.2: Dimensions and Mason Model Parameters of Example PT Design

8.3 Validation Through Simulation

We illustrate this process with an example PT design for $V_{in} = 120\,\mathrm{V}$, $V_{out} = 40\,\mathrm{V}$, and $P_{out} = 100\,\mathrm{W}$. For all material constants, the properties of the APC 841 material (summarized in Table 8.1) are assumed. We also choose $\chi = 1$ and assume $K_B = 0.8$, $\kappa_0 = \pi$, and a loss limit with **respect to the output port** of $1\,\mathrm{W/cm^2}$ (i.e. $H_{max} = \alpha \cdot 1\,\mathrm{W/cm^2}$). Table 8.2 shows the dimensions and parameters of the designed PT, and Fig. 8-4 plots its ZVS region, which shows the nominal operating point is within the ZVS region.

To simulate this design, we derive switching times from the exact periodic steady solution. Details about numerically solving for this solution as well as the MATLAB script can be found in [6]. We use these extracted switching times to simulate the topology shown in Fig. 3-2d in LTspice. (The LTspice schematic can also be found in [6].)

Table 8.3 compares the predicted and simulated performance for the design at the

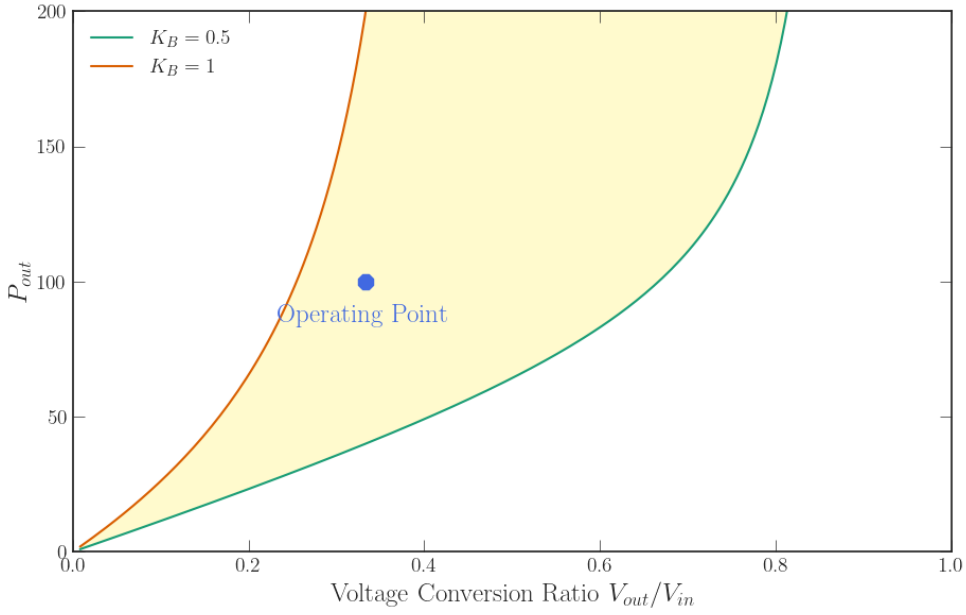

Figure 8-4: ZVS Plot for Example PT Design: Nominal operating point ($V_{in} = 120\,\text{V}$, $V_{out} = 40\,\text{V}$, and $P_{out} = 100\,\text{W}$) is labeled and occurs inside the ZVS region as expected.

Parameter	Design	Simulation
P_{out}	100 W	110 W
f	2.45 MHz	2.17 MHz
η	98.1%	98.4%
I_L	2.62 A	2.64 A

Table 8.3: Design vs. Simulated Performance for Example PT-based Converter

nominal operating point.

The slight deviations in design and simulated values may be attributed to our assumption for $\kappa_0 = \pi$ in the design process. For the k_{33} mode and other "parallel" modes in [8], $\kappa_0 = \pi$ is the geometry-normalized wave number at the antiresonant frequency, which is close to but not exactly the actual operating frequency. [6] and [8] presents a more accurate estimate of κ_0 in the context of PRs.

Fig. 8-5 shows the simulated waveforms for the example PT-based converter operating at the nominal operating point ($V_{in} = 120\,\text{V}$, $V_{out} = 40\,\text{V}$, and $P_{out} = 100\,\text{W}$), reflecting appropriate converter operation. The v_{pA} and v_{pB} waveforms show the converter resonates to the proper connected-stage voltages as defined by its switching

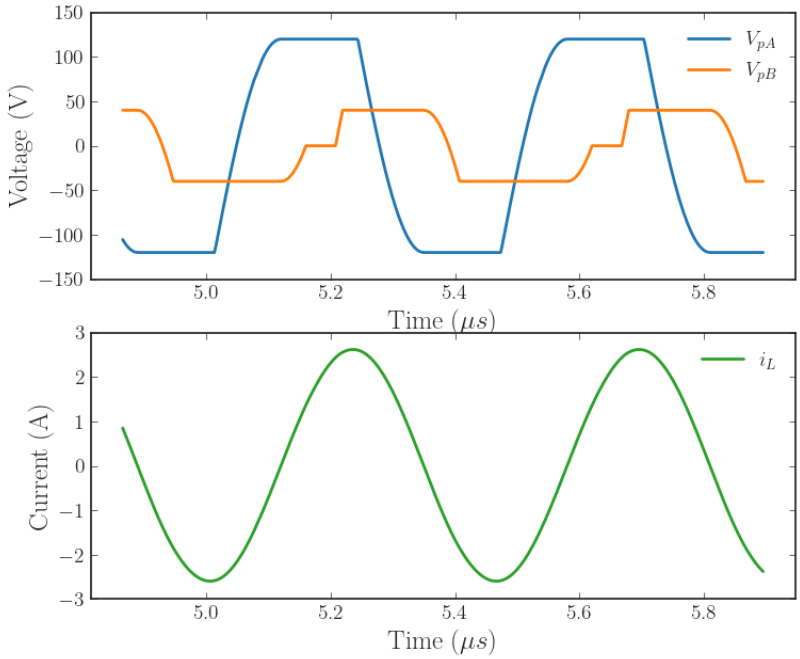

Figure 8-5: Simulated Waveforms for v_{pA}, v_{pB} and i_L for Example PT-based Converter

sequence $V_{in}, -V_{in}|V_{out}, -V_{out}, Zero+$. The i_L plot is nearly sinusoidal and its zero crossings occur at their proper times (at the beginning of the $Zero+$ stage and at the end of V_{out} stage for the output port) according to the switching sequence.

Finally, this design embodies the high-efficiency and high-power-density capabilities of PRs with presently-available PZT materials. This converter achieves an efficiency of 98.4% in simulation, which is significantly higher than the efficiency of the PT-based converter prototype presented in Chapter 3. The volume of this example PT is $0.255\,\mathrm{cm}^3$, which means this theoretical PT design achieves a volumetric power density of $445\,\mathrm{W/cm}^3$. The simulated performance of this design, which combines a high-efficiency switching sequence, its corresponding topology, and a PT component designed to achieve both maximum efficiency and maximum power density, validates the use of both the circuit-level and component-level design strategies presented in this thesis to design high-efficiency, high-power-density PT-based converters.

Chapter 9

Conclusion

Piezoelectric transformers (PTs) offer a number of advantages to power conversion, namely their high power densities and performance capabilities at small scales, over other forms of energy storage such as magnetics. However, many PT-based converter designs in literature that rely on standard converter circuits and commercial PT components fail to fully capitalize on these advantages. In this thesis, we present strategies for designing high-efficiency, high-power-density PT-based DC-DC converters that optimize design on two levels: (1) the circuit level and (2) the component level.

At the circuit level, we enumerate and downselect topologies and switching sequences that effectively utilize the PT for both isolated and non-isolated PT-based dc-dc converters as discussed in Chapter 3. Although these switching sequences add some control complexity compared to standard control sequences, all of the switching sequences presented are capable of high efficiency behaviors including ZVS, all-positive instantaneous power transfer, soft charging of the PT's terminal capacitances, etc. Analysis methods in for predicting the behavior of the converter and estimating its efficiency and ZVS region are also presented in Chapter 2 and 3. We also present an experimental PT-based converter prototype that realizes one of these high-efficiency switching sequences using an off-the-shelf PT component to validate the proposed circuit-level design strategies. With just these circuit-level strategies, this prototype PT-based converter achieves an experimental efficiency of 90%, higher than the effi-

ciencies of many other PT-based converter designs in literature.

At the component level, each dimension of a PT can be optimized for power conversion metrics like efficiency and power density. As presented in Chapter 2, efficiency, power density, and the ZVS region can be calculated using the circuit parameters of the Mason model. Chapter 4 shows how to relate these Mason model parameters to not only the PT's material constants, but also its geometric dimensions under consideration. Finally, we present a process for designing a PT component that can achieve both high efficiency and high power density while maintaining ZVS using the geometry conditions presented in Chapters 5, 6, and 7.

Chapter 8 simulates an example PT-based DC-DC converter design that combines all of the circuit-level and component-level design strategies proposed in this thesis. This converter is able to achieve a modeled efficiency of 98.4% and a modeled power density of $445\,\mathrm{W/cm^3}$, suggesting the value of the combination of high-efficiency switching sequences and geometry conditions for designing high-efficiency, high-power-density PT-based dc-dc converters.

Appendix A

Supplementary Material

A.1 Input-side Transformer Mason Model

In this section, we derive the reduced Mason model with the input-side transformer. Fig. A-1 repeats the circuit before the series RLC network is reflected across one of the transformers for convenience. To arrive at the input-side transformer Mason model, the network must be reflected across the $(\psi : 1)$ transformer. The reflected circuit parameters are given by (A.1).

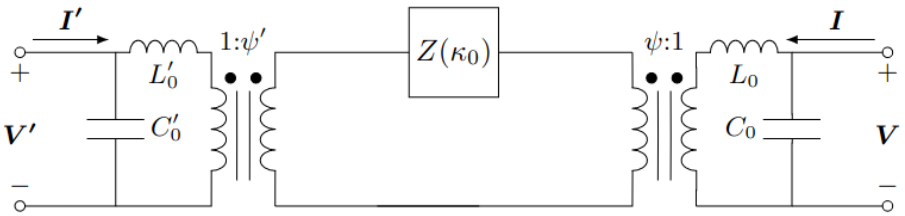

Figure A-1: The impedance network can now be expressed as a single impedance $Z(\kappa_0)$ (repeated for convenience).

$$\begin{aligned} R_{reflected} &= \frac{R_m}{\psi^2} \\ L_{reflected} &= L_0 + \frac{L_m}{\psi^2} + L_0'\Big(\frac{\psi'}{\psi}\Big)^2 \\ C_{reflected} &= C_m\psi^2 \\ N &= \frac{\psi}{\psi'} \end{aligned} \tag{A.1}$$

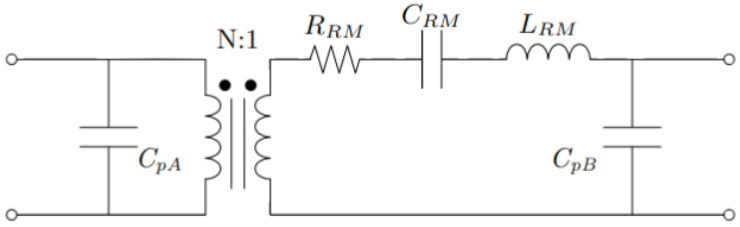

Figure A-2: Mason Model for the $k_{33} - k_{33}$ PT with Input-Side Transformer

Fig. A-2 shows the final reduced Mason model with the input-side transformer with the parameters labeled as ($R_{RM} = R_{reflected}$, $L_{RM} = L_{reflected}$, $C_{RM} = C_{reflected}$, $C_{pA} = C_0'$, and $C_{pB} = C_0$) and given by (A.2).

$$\begin{aligned}
R_{RM} &= \frac{\pi}{8Q_m v_a k_{33}^2 \epsilon_{33}^T (1-k_{33}^2)}(a_1+a_2)\left(\frac{l^2}{a_2^2 b}\right) \\
L_{RM} &= \left(\frac{1}{\omega_0^2}\right)\left(\frac{l}{\epsilon_{33}^T(1-k_{33}^2)a_2 b}\right)\left(1+\frac{a_1}{a_2}+\left(\frac{1}{8k_{33}^2}\right)(a_1+a_2)\left(\frac{\pi^2}{a_2}\right)\right) \\
C_{RM} &= \frac{8k_{33}^2\epsilon_{33}^T(1-k_{33}^2)}{\pi^2}\left(\frac{1}{a_1+a_2}\right)\left(\frac{a_2^2 b}{l}\right) \\
C_{pA} &= \left(\frac{a_1 b}{l}\right)\epsilon_{33}^T(1-k_{33}^2) \\
C_{pB} &= \left(\frac{a_2 b}{l}\right)\epsilon_{33}^T(1-k_{33}^2) \\
N &= \frac{a_2}{a_1}
\end{aligned} \tag{A.2}$$

If we assume the heights of the PRs are related by a scaling factor α such that $a_2 = \alpha a_1$, then (A.2) can be simplifed to (A.3).

$$\begin{aligned}
R_{RM} &= \frac{\pi(1+\alpha)l}{28Q_m v_a k_{33}^2 C_{pA}\alpha^2} \\
L_{RM} &= \frac{1+\alpha}{\omega_0^2 C_{pA}\alpha^2}\left(1+\frac{\pi^2}{8k_{33}^2}\right) \\
C_{RM} &= \frac{8k_{33}^2 C_{pA}\alpha^2}{\pi^2(1+\alpha)} \\
C_{pA} &= \left(\frac{a_1 b}{l}\right)\epsilon_{33}^T(1-k_{33}^2) \\
C_{pB} &= \alpha C_{pA} \\
N &= \alpha
\end{aligned} \tag{A.3}$$

A.2 Minimum Loss Ratio and Geometry Condition with Respect to the Output Port

In this section, we calculate the minimum loss ratio and maximum efficiency geometry condition with respect to the output port. The amplitude of resonance I_L with respect to the output port is:

$$I_{L,out} = \pi N\Big(\frac{P_{out}}{2K_B V_{out}} + \alpha B V_{ppB}\Big) \tag{A.4}$$

The loss ratio with respect to the output port is then:

$$\begin{aligned}\frac{P_{loss}}{P_{out}}\Big|_{out} &= \frac{\frac{1}{2}I_{L,out}^2 R}{P_{out}} \\ &= \frac{\pi^2 R_0(1+\alpha)}{2P_{out}\alpha^2}\left(\frac{P_{out}^2}{4K_B^2 V_{out}^2}\Big(\frac{1}{G}\Big) + \frac{\alpha P_{out} V_{ppB} B_0}{K_B V_{out}} + \alpha^2 G B_0^2 V_{ppB}^2\right)\end{aligned} \tag{A.5}$$

Minimizing (A.5) with respect to the geometry factor G which yields the following minimum loss ratio:

$$\frac{P_{loss}}{P_{out}}\Big|_{out,min} = \frac{\pi^2(1+\alpha)R_0 B_0 V_{ppB}}{\alpha K_B V_{out}} \tag{A.6}$$

which is reached when G is constrained to be:

$$G_{out,efficiency} = \frac{P_{out}}{2\alpha K_B B_0 V_{out} V_{ppB}} \tag{A.7}$$

(A.6) yields the following expression for the peak efficiency with respect to the output port:

$$\eta_{peak} = \Big(1 + \frac{\pi^2(1+\alpha)R_0 B_0 V_{ppB}}{\alpha K_B V_{out}}\Big)^{-1} \tag{A.8}$$

A.3 Power Density Geometry Condition with Respect to the Output Port

This section presents the derivation of the power density geometry condition with respect to the output port.

The power handling capability P_{out} can be expressed in terms of I_L with respect to the output port as:

$$P_{out} = 2K_B V_{out}\left(\frac{I_{L,out}}{\pi N} - \alpha B V_{ppB}\right) \tag{A.9}$$

We explicitly write out the geometry and material terms of $I_{L,out}$ as:

$$I_{L,out} = I_{Lmax0}\left(\frac{a_2 b}{l}\right) = I_{Lmax0}\left(\frac{ab}{Nl}\right) \tag{A.10}$$

where I_{Lmax0} can be calculated using (7.11). Substituting this in (A.9) and simplifying yields:

$$P_{out} = \frac{2K_B V_{out}}{N}\left(\frac{ab}{l}\right)\left(\frac{I_{Lmax0}}{\pi N} - \frac{B_0 V_{ppB}}{l}\right) \tag{A.11}$$

Energy handling density is defined to be $\frac{E_{out}}{\text{vol}} = \frac{P_{out}}{\text{vol}\cdot f}$. vol and f are:

$$\begin{aligned} \text{vol} &= \frac{abl(N+1)}{N} \\ f &= \frac{\kappa_0 v_a}{2\pi l} \end{aligned} \tag{A.12}$$

respectively. Thus, energy handling density is:

$$\begin{aligned} \frac{E_{out}}{\text{vol}} &= \frac{2K_B V_{out}}{l^2(1+N)}\left(\frac{I_{Lmax0}}{\pi} - \frac{B_0 V_{ppB}}{l}\right)\left(\frac{2\pi l}{\kappa_0 v_a}\right) \\ &= \frac{4K_B V_{out}\pi}{\kappa_0 v_a(1+N)}\left(\frac{I_{Lmax0}}{\pi N l} - \frac{B_0 V_{ppB}}{l^2}\right) \end{aligned} \tag{A.13}$$

(A.13) is maximized at an optimized length of:

$$l_{power} = \frac{2\pi N B_0 V_{ppB}}{I_{Lmax0}} \tag{A.14}$$

which gives a maximum energy handling density of:

$$\left.\frac{E_{out}}{\text{vol}}\right|_{max} = \frac{K_B V_{out} I_{Lmax0}^2}{\pi \kappa_0 v_a B_0 V_{ppA}(1+N)N^2} \tag{A.15}$$

A.4 Python Script for PT Design

```
import matplotlib.pyplot as plt
from math import pi
import numpy as np
import matplotlib as mpl
from pylab import cm
import pandas as pd

# This script assumes the Vin, -Vin | Vout, -Vout, Zero+ switching
    sequence
# Designs a PT, plots the ZVS region for the design,
# and estimates peak efficiency and power density for design

########################## PARAMETERS FOR USER TO CHANGE
    ##########################
# Parameters to Adjust for PT Design
Vin_d = 120          # design Vin (CAN CHANGE)
Vout_d = 40         # design Vout (CAN CHANGE)
Pout_d = 100         # design Pout (CAN CHANGE)
chi = 1              # chi = Pout/Pout_min (CAN CHANGE)
KB_d = 0.8           # design KB (CAN CHANGE)

# Parameters to Adjust for Operating
Vin_o = Vin_d        # operating Vin should equal Vin_d for this
    switching sequence
Vout_o = Vout_d      # operating Vout (CAN CHANGE)
Pout_o = Pout_d      # operating Pout (CAN CHANGE)


########################## DO NOT CHANGE ANYTHING AFTER HERE
```

```
    ####################
# Constants
kappa0 = pi          # CHANGE if kappa0 =/= pi
KA = 1
rho = 7.6*1000
d33 = 300e-12
k33 = 0.68
Y33 = 6.3e10
s33E = 1/Y33
s33D = s33E*(1-k33**2)
e33S = (1-k33**2)*1375*8.854e-12
e33T = e33S/(1-k33**2)
va = 1/(rho*s33D)**0.5
Qm = 1400
print('Printing Material Properties...')
print(f'rho: {rho}')
print(f'e33T: {e33T}')
print(f's33E: {s33E}')
print(f's33D: {s33D}')
print(f'va: {va}')
print(f'k33: {k33}')
print(f'Qm: {Qm}')
print(f'e33s: {e33T*(1-k33**2)}')
print()

B0 = kappa0*va*e33T*(1-k33**2)/(2*pi)
R0 = pi/(8*Qm*va*k33**2*e33T*(1-k33**2))

################################### PT Design
    ################################
def design_PT(Vin_d, Vout_d, Pout_d, chi, KB_d):
    """Returns the Mason model parameters for a PT design

    PT is designed using the efficiency, ZVS, power density geometry
    conditions.

```

```
    Parameters
    ----------
    Vin_d : float
        Design operating Vin
    Vout_d : float
        Design operating Vout
    Pout_d : float
        Design operating Pout
    chi : float
        Fraction of Pout at which ZVS is lost (chi = Pout/P_{out,min})
    KB_d : float
        Desired KB in the middle of 0.5<KB<1

    Returns
    -------
    tuple
        The Mason model circuit parameters
        (N, CpA, CpB, Crm, Lrm, Rrm, f)
    """
    VppA_d = 2*Vin_d
    VppB_d = 2*Vout_d

    # PT dimensions
    print('Calculating PT Dimensions...')
    # Solve for alpha
    alpha = chi*KA*Vin_d*VppA_d/(KB_d*Vout_d*(VppA_d*(chi+1)-VppB_d))
    print(f'alpha = {alpha}')

    # Solve for l
    Hmax = alpha*10000                      # loss density wrt output
    ILmax0 = (2*Hmax/(R0*(1+alpha)))**0.5
    l = 2*pi*B0*VppA_d/(ILmax0)
    # print(f'ILmax0: {ILmax0}')
```

```
    print(f'l = {l}')

    # Solve for G
    G = Pout_d/(2*KA*B0*Vin_d*VppA_d)
    print(f'G = {G}')

    # Assume a=b, solve for a
    a = l*G**0.5
    b = a
    print(f'a = b = {a}')
    vol = a*b*l*(1+alpha)
    print(f'Volume = {vol}')
    print()

    # PT circuit parameters
    print('Calculating PT Circuit Parameters...')
    omega0 = pi*va/l
    N = 1/alpha
    CpA = e33T*(1-k33**2)*(a*b)/l
    CpB = alpha*CpA
    Crm = 8*k33**2*CpA/(pi**2*(1+alpha))
    Lrm = (1+alpha)/(omega0**2*CpA)*(1+(pi**2/(8*k33**2)))
    Rrm = pi*(1+alpha)*l/(8*Qm*va*k33**2*CpA)

    f = kappa0*va/(2*pi*l)


    print(f'N = {N};')
    print(f'CpA in [F] = {CpA};')
    print(f'CpB in [F] = {CpB};')
    print(f'Crm in [F] = {Crm};')
    print(f'Lrm in [H] = {Lrm};')
    print(f'Rrm in [Ohm] = {Rrm};')
    print(f'f in [Hz] = {f};')
    print()
    return (N, CpA, CpB, Crm, Lrm, Rrm, f, vol)
```

```
129
130 ######################## Peak Efficiency Estimation
    ############################
131 def peak_eff_estimate(N, Vin):
132     """Returns the peak efficiency which should only depend on N and
    Vin
133
134     For this switching sequence Vin should be constant.
135
136     Parameters
137     ----------
138     N : float
139         N = 1/alpha, turns ratio
140     Vin : float
141         Operating Vin = Vin_d for this switching sequence
142     """
143     alpha = 1/N
144     VppA = 2*Vin
145     LR = pi**2*(1+alpha)*R0*B0*VppA/(KA*Vin)
146     return 1/(1+LR)
147
148 ################################## Plot ZVS region
    ############################
149 plt.style.use('seaborn-white')
150
151 tex_fonts = {
152     # Use LaTeX to write all text
153     "text.usetex": True,
154     "font.family": "serif",
155     # Use 10pt font in plots, to match 10pt font in document
156     "axes.labelsize": 18,
157     "font.size": 18,
158     # Make the legend/label fonts a little smaller
159     "legend.fontsize": 14,
160     "xtick.labelsize": 14,
161     "ytick.labelsize": 14,
```

```
}

plt.rcParams.update(tex_fonts)


def plot_zvs(CpA, CpB, f, N, Vin, Vout, Pout):
    """ Plots the ZVS region given parameters of a PT

    Parameters
    ----------
    CpA : float
    CpB : float
    f : float
    N : float
    Vin : float
        operating Vin, which should equal design Vin
    Vout : float
        operating Vout, which can be different from design Vout
    Pout : float
        operating Pout, which can be different from design Pout
    """
    print('Plotting ZVS Region...')
    fig, ax = plt.subplots(1, 1)
    colors = cm.get_cmap('Dark2')

    delta = 1e-5
    VppA = 2*Vin
    KBmin = 0.5+delta
    KBmax = 1-delta

    Vo = np.linspace(1,Vin,200)
    VppB = 2*Vo
    Vor = np.linspace(N*Vin-1, Vin, 100)
    VppBr = 2*Vor
    top = np.full(np.shape(Vor), np.inf)

```

```
198     P1 = (2*N*CpB*VppB-2*CpA*VppA)/(1/(f*KA*Vin) - N/(f*KBmin*Vo))
199     P2 = (2*N*CpB*VppB-2*CpA*VppA)/(1/(f*KA*Vin) - N/(f*KBmax*Vo))
200     P3 = (2*N*CpB*VppBr-2*CpA*VppA)/(1/(f*KA*Vin) - N/(f*KBmin*Vor))
201
202     P1 = np.where(P1 < 0, np.NAN, P1)
203     P2 = np.where(P2 < 0, np.NAN, P2)
204     P3 = np.where(P3 < 0, np.NAN, P3)
205
206     # Plot ZVS boundaries (x-axis = v ratio)
207     ax.plot(Vo/Vin, P1, color=colors(0), label="$K_B=0.5$", zorder
    =0)
208     ax.plot(Vo/Vin, P2, color=colors(1), label="$K_B=1$")
209     ax.fill_between(Vo/Vin, P1, P2, color='lemonchiffon', zorder=-1)
210     ax.fill_between(Vor/Vin, P3, 2000, color='lemonchiffon', zorder
    =-1)
211     ax.set_xlabel("Voltage Conversion Ratio $V_{out}/V_{in}$")
212
213     # Plot ZVS boundaries (x-axis = Vout)
214     # ax.plot(Vo, P1, color=colors(0), label="$KB_{min}=0.5$")
215     # ax.plot(Vo, P2, color=colors(1), label="$KB_{max}=1$")
216     # ax.plot(Vo, P3, color=colors(2), label="$KB=0.68$")
217     # ax.set_xlabel("$V_{out}$")
218
219     # Plot Operating Point
220     ax.scatter([Vout/Vin],[Pout], s=120, marker='8', color='
    royalblue')
221     ax.annotate('Operating Point', (Vout/Vin-0.1,Pout-0.15*Pout),
    zorder=2, color='royalblue' )
222
223     ax.set_ylim(0,2*Pout)
224     ax.set_xlim(0,1)
225     xtick_locs = [0.2*i for i in range(6)]
226     ytick_locs = [2*Pout/4*i for i in range(5)]
227     ax.set_xticks(xtick_locs)
228     ax.set_yticks(ytick_locs)
229     ax.xaxis.set_tick_params(which='major', size=8, width=0.5,
```

```
    direction='in', top='on', right='on')
230     ax.yaxis.set_tick_params(which='major', size=8, width=0.5,
    direction='in', top='on', right='on')
231
232     ax.set_ylabel("$P_{out}$")
233     plt.legend()
234     plt.show()
235
236 ########################## FUNCTION CALLS
    ######################################
237
238 # Design a PT
239 print(f'Printing Design Point...')
240 print(f'Vin_d = {Vin_d}')
241 print(f'Vout_d = {Vout_d}')
242 print(f'Pout_d = {Pout_d}')
243 print(f'chi = {chi}')
244 print(f'KB_d = {KB_d}')
245 print()
246 N, CpA, CpB, Crm, Lrm, Rrm, f , vol = design_PT(Vin_d, Vout_d,
    Pout_d, chi, KB_d)
247
248 # print for Spice simulation
249 print(f'Printing for Parameters in Spice Simulation...')
250 print(f'.param Rrm = {Rrm}')
251 print(f'.param Crm = {Crm}')
252 print(f'.param Lrm = {Lrm}')
253 print(f'.param CpA = {CpA}')
254 print(f'.param CpB = {CpB}')
255 print(f'.param N = {N}')
256 print()
257
258 # print for MATLAB simulation
259 print(f'Printing for Parameters in MATLAB Simulation...')
260 print(f'CpA = {CpA};')
261 print(f'CpBo = {CpB};')
```

```
262 print(f'L = {Lrm};')
263 print(f'C = {Crm};')
264 print(f'R = {Rrm};')
265 print(f'N = {N};')
266 print()
267
268 # estimate performance
269 eff = peak_eff_estimate(N, Vin_o)
270 print('Estimating Performance...')
271 print(f'Estimated Peak Efficiency: {eff}')
272 print(f'Estimated IL in [A]: {pi*(Pout_o/(2*KA*Vin_d)+2*f*CpA*Vin_d)
       }')
273 print(f'Estimated Power Density in [W/cm^3]: {Pout_o/vol*1e-6}')
274 print()
275
276 # for plotting
277 plot_zvs(CpA, CpB, f, N, Vin_o, Vout_o, Pout_o)
```

Bibliography

[1] “Equivalent circuit parameters for piezo transformers".

[2] “Physical and piezoelectric properties of APC materials".

[3] J Marcos Alonso, Carlos Ordiz, and Marco A Dalla Costa. A novel control method for piezoelectric-transformer based power supplies assuring zero-voltage-switching operation. *IEEE Transactions on Industrial Electronics*, 55(3):1085–1089, 2008.

[4] Shmuel Ben-Yaakov and Simon Lineykin. Maximum power tracking of piezoelectric transformer hv converters under load variations. *IEEE Transactions on power electronics*, 21(1):73–78, 2006.

[5] Fabio E Bisogno, M Radecker, A Knoll, A Vazquez Carazo, A Riedlhammer, G Deboy, N Norvez, and JM Pacas. Comparison of resonant topologies for step-down applications using piezoelectric transformers. In *2004 IEEE 35th Annual Power Electronics Specialists Conference (IEEE Cat. No. 04CH37551)*, volume 4, pages 2662–2667. IEEE, 2004.

[6] Jessica D Boles. *Power Electronics Meet Piezoelectrics: Converters, Components, and Miniaturization*. PhD thesis, Massachusetts Institute of Technology, 2022.

[7] Jessica D Boles, Pedro L Acosta, Yogesh K Ramadass, Jeffrey H Lang, and David J Perreault. Evaluating piezoelectric materials for power conversion. In *Proc. IEEE Workshop on Control and Modeling for Power Electronics*, pages 1–8, Aalborg, Denmark, November 2020.

[8] Jessica D Boles, Joseph E Bonavia, Pedro L Acosta, Yogesh K Ramadass, Jeffrey H Lang, and David J Perreault. Enumeration and analysis of dc-dc converter implementations based on piezoelectric resonators. *IEEE Transactions on Power Electronics*, 37(3):3374–3390, 2022.

[9] Jessica D Boles, Elaine Ng, Jeffrey H Lang, and David J Perreault. Dc-dc converter implementations based on piezoelectric transformers. *IEEE Journal of Emerging and Selected Topics in Power Electronics*, 2022.

[10] Jessica D Boles, Joshua J Piel, and David J Perreault. Analysis of high-efficiency operating modes for piezoelectric resonator-based dc-dc converters. In *Proc. IEEE Applied Power Electronics Conference and Exposition*, pages 1–8, New Orleans, LA, USA, March 2020.

[11] Jessica D Boles, Joshua J Piel, and David J Perreault. Enumeration and analysis of dc-dc converter implementations based on piezoelectric resonators. *IEEE Transactions on Power Electronics*, 36(1):129–145, 2021.

[12] Svetlana Bronstein and Sam Ben-Yaakov. Design considerations for achieving ZVS in a half bridge inverter that drives a piezoelectric transformer with no series inductor. In *Proc. IEEE Power Electronics Specialists Conference*, volume 2, pages 585–590, Cairns, Queensland, Australia, June 2002.

[13] Shih-Yu Chen and Chern-Lin Chen. ZVS considerations for a phase-lock control dc/dc converter with piezoelectric transformer. In *Proc. Annual Conference of the IEEE Industrial Electronics Society*, pages 2244–2248, Paris, France, November 2006.

[14] Enrico Dallago, Albert Danioni, Marco Passoni, and Giuseppe Venchi. Modelling of dc-dc converter based on a piezoelectric transformer and its control loop. In *2002 IEEE 33rd Annual IEEE Power Electronics Specialists Conference. Proceedings (Cat. No. 02CH37289)*, volume 2, pages 927–931. IEEE, 2002.

[15] Juan Díaz, Fernando Nuño, Juan Manuel Lopera, and Juan Antonio Martín-Ramos. A new control strategy for an ac/dc converter based on a piezoelectric transformer. *IEEE Transactions on Industrial Electronics*, 51(4):850–856, 2004.

[16] Juan Diaz, Fernando Nuno, Miguel J Prieto, Juan A Martin-Ramos, and Pedro José Villegas Saiz. Closing a second feedback loop in a dc–dc converter based on a piezoelectric transformer. *IEEE transactions on power electronics*, 22(6):2195–2201, 2007.

[17] Shuxiang Dong, Alfredo Vazquez Carazo, and Seung Ho Park. Equivalent circuit and optimum design of a multilayer laminated piezoelectric transformer. *IEEE transactions on ultrasonics, ferroelectrics, and frequency control*, 58(12):2504–2515, 2011.

[18] Marzieh Ekhtiari, Thomas Andersen, Michael AE Andersen, and Zhe Zhang. Dynamic optimum dead time in piezoelectric transformer-based switch-mode power supplies. *IEEE Transactions on Power Electronics*, 32(1):783–793, 2017.

[19] Marzieh Ekhtiari, Zhe Zhang, and Michael AE Andersen. Analysis of bidirectional piezoelectric-based converters for zero-voltage switching operation. *IEEE Transactions on Power Electronics*, 32(1):866–877, 2017.

[20] Marzieh Ekhtiari, Tiberiu-Gabriel Zsurzsan, Michael AE Andersen, and Zhe Zhang. Optimum phase shift in the self-oscillating loop for piezoelectric-transformer-based power converters. *IEEE Transactions on Power Electronics*, 33(9):8101–8109, 2017.

[21] Jack Forrester, Jonathan Davidson, Martin Foster, and David Stone. Radptdesigner: A program for designing radial mode piezoelectric transformers for inductorless inverters. In *Proc. IEEE European Conference on Power Electronics and Applications (EPE'21 ECCE Europe)*, pages 1–7, Ghent, Belgium, September 2021. IEEE.

[22] Jack Forrester, Jonathan Neil Davidson, Martin P Foster, and David A Stone. Influence of spurious modes on the efficiency of piezoelectric transformers: A sensitivity analysis. *IEEE Transactions on Power Electronics*, 36(1):617–629, 2020.

[23] Martin P Foster, Jonathan N Davidson, Edward L Horsley, and David A Stone. Critical design criterion for achieving zero voltage switching in inductorless half-bridge-driven piezoelectric-transformer-based power supplies. *IEEE Transactions on Power Electronics*, 31(7):5057–5066, 2015.

[24] Sunao Hamamura, Daisuke Kurose, Tamotsu Ninomiya, and Mitsuru Yamamoto. New control method of piezoelectric transformer converter by pwm and pfm for wide range of input voltage. In *7th IEEE International Power Electronics Congress. Technical Proceedings. CIEP 2000 (Cat. No. 00TH8529)*, pages 3–8. IEEE, 2000.

[25] Alex J Hanson, Julia A Belk, Seungbum Lim, Charles R Sullivan, and David J Perreault. Measurements and performance factor comparisons of magnetic materials at high frequency. *IEEE Transactions on Power Electronics*, 31(11):7909–7925, 2016.

[26] Edward L Horsley, Alfredo V Carazo, Nam Nguyen-Quang, Martin P Foster, and David A Stone. Analysis of inductorless zero-voltage-switching piezoelectric transformer-based converters. *IEEE Transactions on Power Electronics*, 27(5):2471–2483, 2012.

[27] EL Horsley, MP Foster, and DA Stone. State-of-the-art piezoelectric transformer technology. In *2007 European Conference on Power Electronics and Applications*, pages 1–10. IEEE, 2007.

[28] Gregory Ivensky, Svetlana Bronstein, and Shmuel Ben-Yaakov. A comparison of piezoelectric transformer ac/dc converters with current doubler and voltage doubler rectifiers. *IEEE transactions on power electronics*, 19(6):1446–1453, 2004.

[29] Gregory Ivensky, Isaac Zafrany, and Sam Ben-Yaakov. Generic operational characteristics of piezoelectric transformers. *IEEE Transactions on Power Electronics*, 17(6):1049–1057, 2002.

[30] Bin Ju, Liang Fang, Qing Wang, Jiawen Xu, Guoli Li, and Yongbin Liu. General rules for the inductive characteristics of a piezoelectric structure and its integration with piezoelectric transformer for capacitive compensation. *Smart Materials and Structures*, 30(4):1–16, 2021.

[31] Bin Ju, Weiwei Shao, and Zhihua Feng. Piezoelectric filter module used in harmonics elimination for high-efficiency piezoelectric transformer driving. *IEEE Transactions on Power Electronics*, 31(1):524–532, 2015.

[32] Bin Ju, Weiwei Shao, Liansheng Zhang, Hongbo Wang, and Zhihua Feng. Piezoelectric ceramic acting as inductor for capacitive compensation in piezoelectric transformer. *IET Power Electronics*, 8(10):2009–2015, 2015.

[33] Bin Ju, Qing Wang, Liang Fang, Fang Liu, Guoli Li, and Yongbin Liu. Single-layer piezoelectric transformers with a unique design of polarization topologies. *Sensors and Actuators A: Physical*, 332:113193, 2021.

[34] Mudit Khanna, Rolando Burgos, Qiong Wang, Khai DT Ngo, and Alfredo Vazquez Carazo. New tunable piezoelectric transformers and their application in dc–dc converters. *IEEE Transactions on Power Electronics*, 32(12):8974–8978, 2017.

[35] Phyo Aung Kyaw, Aaron LF Stein, and Charles R Sullivan. Fundamental examination of multiple potential passive component technologies for future power electronics. *IEEE Transactions on Power Electronics*, 33(12):10,708–10,722, 2018.

[36] Xiaotian Li, Deepam Maurya, Alfredo V Carazo, Mohan Sanghadasa, and Shashank Priya. Tunable high-power multilayer piezoelectric transformer. *IEEE Transactions on Industrial Electronics*, 67(10):8335–8343, 2019.

[37] Yunxiu Li and Wei Chen. Ac-dc converter with worldwide range input voltage by series and parallel piezoelectric transformer connection. In *2004 IEEE 35th Annual Power Electronics Specialists Conference (IEEE Cat. No. 04CH37551)*, volume 4, pages 2668–2671. IEEE, 2004.

[38] Chih-yi Lin. *Design and analysis of piezoelectric transformer converters*. PhD thesis, Virginia Tech, 1997.

[39] CY Lin and FC Lee. Design of a piezoelectric transformer converter and its matching networks. In *Proceedings of 1994 Power Electronics Specialist Conference-PESC'94*, volume 1, pages 607–612. IEEE, 1994.

[40] Ray L Lin, Fred C Lee, Eric M Baker, and Dan Y Chen. Inductor-less piezoelectric transformer electronic ballast for linear fluorescent lamp. In *Proc. IEEE Applied Power Electronics Conference and Exposition*, pages 664–669, Anaheim, CA, USA, March 2001.

[41] Yuan-Ping Liu, Dejan Vasic, François Costa, Wen-Jong Wu, and Chih-Kung Lee. Design of fixed frequency controlled radial-mode stacked disk-type piezoelectric transformers for dc/dc converter applications. *Smart Materials and Structures*, 18(8):085025, 2009.

[42] Yuan-Ping Liu, Dejan Vasic, François Costa, Wen-Jong Wu, and Denis Schwander. Fixed frequency controlled piezoelectric 10w dc/dc converter. In *2010 IEEE Energy Conversion Congress and Exposition*, pages 3030–3037. IEEE, 2010.

[43] Juan A Martin-Ramos, Miguel Angel Jose Prieto, F Nuño García, J Diaz González, and FM Fernndez Linera. A new full-protected control mode to drive piezoelectric transformers in dc-dc converters. *IEEE Transactions on Power Electronics*, 17(6):1096–1103, 2002.

[44] Warren P Mason. *Electromechanical Transducers and Wave Filters*. D. Van Nostrand Co., 1948.

[45] Kaspar Sinding Meyer, Michael AE Andersen, and Flemming Jensen. Parameterized analysis of zero voltage switching in resonant converters for optimal electrode layout of piezoelectric transformers. In *2008 IEEE Power Electronics Specialists Conference*, pages 2543–2548. IEEE, 2008.

[46] J Navas, T Bove, JA Cobos, F Nuno, and K Brebol. Miniaturised battery charger using piezoelectric transformers. In *APEC 2001. Sixteenth Annual IEEE Applied Power Electronics Conference and Exposition (Cat. No. 01CH37181)*, volume 1, pages 492–496. IEEE, 2001.

[47] Elaine Ng, Jessica D. Boles, Jeffrey H. Lang, and David J. Perreault. Non-isolated dc-dc converter implementations based on piezoelectric transformers. In *2021 IEEE Energy Conversion Congress and Exposition (ECCE)*, pages 1749–1756, 2021.

[48] Sadachai Nittayarumphong, Fabio Bisogno, Matthias Radecker, Alois Knoll, Alfredo Vazquez Carazo, and Anton Riedlhammer. Dynamic behaviour of pi controlled class-e resonant converter for step-down applications using piezoelectric transformers. In *2005 European Conference on Power Electronics and Applications*, pages 10–pp. IEEE, 2005.

[49] Osamu Ohnishi, H Kishie, A Iwamoto, Y Sasaki, T Zaitsu, and T Inoue. Piezoelectric ceramic transformer operating in thickness extensional vibration mode for power supply. In *IEEE 1992 Ultrasonics Symposium Proceedings*, pages 483–488. IEEE, 1992.

[50] Joung-hu Park, Sungjin Choi, Sangmin Lee, and Bo H Cho. Gain-adjustment technique for resonant power converters with piezoelectric transformer. In *2007 IEEE Power Electronics Specialists Conference*, pages 2549–2553. IEEE, 2007.

[51] David J Perreault, Jingying Hu, Juan M Rivas, Yehui Han, Olivia Leitermann, Robert CN Pilawa-Podgurski, Anthony Sagneri, and Charles R Sullivan. Opportunities and challenges in very high frequency power conversion. In *Proc. IEEE Applied Power Electronics Conference and Exposition*, pages 1–14, Washington, DC, USA, February 2009.

[52] Joshua J Piel. Closed loop control for a piezoelectric-resonator-based dc-dc power converter. Master's thesis, Massachusetts Institute of Technology, February 2022.

[53] A. Rand. Inductor size vs. Q: A dimensional analysis. *IEEE Transactions on Component Parts*, 10(1):31–35, 1963.

[54] Martin S Rødgaard. Bi-directional piezoelectric transformer based converter for high-voltage capacitive applications. In *Proc. IEEE Applied Power Electronics Conference and Exposition*, pages 1993–1998, Charlotte, NC, USA, March 2015.

[55] Martin S Rødgaard, Michael Weirich, and Michael AE Andersen. Forward conduction mode controlled piezoelectric transformer-based pfc led drive. *IEEE Transactions on Power Electronics*, 28(10):4841–4849, 2012.

[56] MS Rodgaard, MA Andersen, and E Bruun. Piezoelectric transformer based power converters; design and control. *Technical Univ. of Denmark, Dep. of Electrical Engineering*, 2012.

[57] MS Rodgaard, Thomas Andersen, and Michael AE Andersen. Empiric analysis of zero voltage switching in piezoelectric transformer based resonant converters. In *Proc. IET International Conference on Power Electronics, Machines and Drives*, Bristol, UK, March 2012.

[58] Myounghwan Ryu, Sungjin Choi, Sangmin Lee, and Bo H Cho. A new piezoelectric transformer driving topology for universal input ac/dc adapter using a constant frequency pwm control. In *Twenty-First Annual IEEE Applied Power Electronics Conference and Exposition, 2006. APEC'06.*, pages 4–pp. IEEE, 2006.

[59] Almudena M Sánchez, Marina Sanz, Roberto Prieto, Jesús A Oliver, Pedro Alou, and José A Cobos. Design of piezoelectric transformers for power converters by means of analytical and numerical methods. *IEEE transactions on industrial electronics*, 55(1):79–88, 2008.

[60] M Sanz, P Alou, A Soto, R Prieto, JA Cobos, and J Uceda. Magnetic-less converter based on piezoelectric transformers for step-down dc/dc and low power application. In *Proc. IEEE Applied Power Electronics Conference and Exposition*, pages 615–621, Miami Beach, FL, USA, February 2003.

[61] Charles R Sullivan, Bradley A Reese, Aaron LF Stein, and Phyo Aung Kyaw. On size and magnetics: Why small efficient power inductors are rare. In *Proc. IEEE Intl. Symposium on 3D Power Electronics Integration and Manufacturing*, pages 1–23, Raleigh, NC, USA, June 2016.

[62] Dejan Vasic, Yuan-Ping Liu, François Costa, and Denis Schwander. Piezoelectric transformer-based dc/dc converter with improved burst-mode control. In *2013 IEEE Energy Conversion Congress and Exposition*, pages 140–146. IEEE, 2013.

[63] Alfredo Vazquez Carazo. Piezoelectric transformers: An historical review. In *Actuators*, volume 5. MDPI, 2016.

[64] Le Wang, Rolando P Burgos, and Alfredo Vazquez Carazo. Design and analysis of tunable piezoelectric transformer based dc/dc converter with ac output inductor. In *2020 IEEE Applied Power Electronics Conference and Exposition (APEC)*, pages 1398–1403. IEEE, 2020.

[65] Le Wang, Keyao Sun, and Rolando Burgos. Planar piezoelectric transformer-based high step-down voltage-ratio dc-dc converter. *IEEE Transactions on Power Electronics*, 2022.

[66] Le Wang, Qiong Wang, Rolando P. Burgos, Khai D. T. Ngo, and Alfredo Carazo Vazquez. A comparison of dc and ac output inductors in tunable piezoelectric transformer based dc/dc converters. In *Proc. IEEE Energy Conversion Congress and Exposition*, Baltimore, MD, USA, September 2019.

[67] Le Wang, Qiong Wang, Mudit Khanna, Rolando P Burgos, Khai DT Ngo, and Alfredo VazquezCarazo. Design and control of tunable piezoelectric transformer based dc/dc converter. In *2018 IEEE Energy Conversion Congress and Exposition (ECCE)*, pages 5987–5993, Portland, OR, USA, September 2018.

[68] Takashi Yamane, Sunao Hamamura, Toshiyuki Zaitsu, T Minomiya, Masahito Shoyama, and Yoshiaki Fuda. Efficiency improvement of piezoelectric-transformer dc-dc converter. In *PESC 98 Record. 29th Annual IEEE Power Electronics Specialists Conference (Cat. No. 98CH36196)*, volume 2, pages 1255–1261. IEEE, 1998.

[69] Yujia Yang, Fabio E Bisogno, Andressa Schittler, Sadachai Nittayarumphong, Matthias Radecker, Wolf-Joachim Fischer, and Marc Fahlenkamp. Comparison of inductor-half-bridge and class-e resonant topologies for piezoelectric transformer applications. In *2009 IEEE Energy Conversion Congress and Exposition*, pages 776–782. IEEE, 2009.

[70] Zijiang Yang, Jack Forrester, Jonathan N Davidson, Martin P Foster, and David A Stone. Resonant current estimation and phase-locked loop feedback design for piezoelectric transformer-based power supplies. *IEEE Transactions on Power Electronics*, 35(10):10466–10476, 2020.

[71] ST Yun, JM Sim, JH Park, SJ Choi, and BH Cho. Adaptive phase control method for load variation of resonant converter with piezoelectric transformer. In *2007 7th International Conference on Power Electronics and Drive Systems*, pages 164–168. IEEE, 2007.

[72] Toshiyuki Zaitsu, O Ohnishi, T Inoue, M Shoyama, T Ninomiya, FC Lee, and GC Hua. Piezoelectric transformer operating in thickness extensional vibration and its application to switching converter. In *Proceedings of 1994 Power Electronics Specialist Conference-PESC'94*, volume 1, pages 585–589. IEEE, 1994.

[73] Weiping Zhang, Dongyan Zhang, Yuhua Wang, Yaai Chen, Yuanchao Liu, and Jing Cao. A low-cost-zvs-class-e converter using pt. In *2004 IEEE 35th Annual Power Electronics Specialists Conference (IEEE Cat. No. 04CH37551)*, volume 3, pages 1803–1807. IEEE, 2004.

[74] Weiping Zhang, Xiaoqiang Zhang, Yuzhou Lei, and Yuanchao Liu. Narrow-control-bandwidth operation of piezoelectric-transformer converter. In *2007 7th International Conference on Power Electronics and Drive Systems*, pages 1628–1632. IEEE, 2007.